Article

Autonomous self-burying seed carriers for aerial seeding

https://doi.org/10.1038/s41586-022-05656-3

Received: 9 February 2022

Accepted: 14 December 2022

Published online: 15 February 2023

Check for updates

Danli Luo[1], Aditi Maheshwari[2], Andreea Danielescu[2], Jiaji Li[3], Yue Yang[3], Ye Tao[4], Lingyun Sun[3], Dinesh K. Patel[1], Guanyun Wang[1,3]✉, Shu Yang[5]✉, Teng Zhang[6,7]✉ & Lining Yao[1]✉

Aerial seeding can quickly cover large and physically inaccessible areas[1] to improve soil quality and scavenge residual nitrogen in agriculture[2], and for postfire reforestation[3–5] and wildland restoration[6,7]. However, it suffers from low germination rates, due to the direct exposure of unburied seeds to harsh sunlight, wind and granivorous birds, as well as undesirable air humidity and temperature[1,8,9]. Here, inspired by *Erodium* seeds[10–14], we design and fabricate self-drilling seed carriers, turning wood veneer into highly stiff (about 4.9 GPa when dry, and about 1.3 GPa when wet) and hygromorphic bending or coiling actuators with an extremely large bending curvature (1,854 m^{-1}), 45 times larger than the values in the literature[15–18]. Our three-tailed carrier has an 80% drilling success rate on flat land after two triggering cycles, due to the beneficial resting angle (25°–30°) of its tail anchoring, whereas the natural *Erodium* seed's success rate is 0%. Our carriers can carry payloads of various sizes and contents including biofertilizers and plant seeds as large as those of whitebark pine, which are about 11 mm in length and about 72 mg. We compare data from experiments and numerical simulation to elucidate the curvature transformation and actuation mechanisms to guide the design and optimization of the seed carriers. Our system will improve the effectiveness of aerial seeding to relieve agricultural and environmental stresses, and has potential applications in energy harvesting, soft robotics and sustainable buildings.

Hygroscopic seeds of various natural grass species are known for their self-burial behaviours, in which the awns respond to variations in external humidity, causing the seed tip to self-bury[10–14,19]. These behaviours are advantageous, allowing seeds to avoid fire[20], and reducing both exposure to high temperature[21] and sensitivity to precipitation. However, the seed morphology is often evolved to tailor to specific natural habitat[22] and other physical constraints, with little flexibility for customization. There is no guarantee that a chosen type will work for the target habitat and payloads. The hygroscopic seeds of *Erodium*, *Stipa* and *Aristida* achieved almost zero anchoring on relatively flat terrain after three triggering cycles in a controlled test (Supplementary Video 1 and Supplementary Note 1). Additionally, many hygroscopic grass seeds have lightweight seedpods (for example, about 8 to about 20 mg; Supplementary Table 1), thus limiting the potential to carry heavier payloads such as the approximately 72-mg whitebark pine seeds, which are important for reforestation[4,23]. An engineered replica of the *Erodium* seed has been demonstrated for field sensor deployment[24]. However, a 0–20% establishment rate after the first actuation cycle, the limited soil types requiring artificial crevices, and the long chemical washing cycles in manufacturing (7 h) limit its potential application in aerial seeding. Clearly, this gap opens an opportunity to design and engineer self-burying systems. Here we set three design criteria: they should work robustly on both flat and rough terrains; the overall size and other geometrical factors should be tunable to accommodate a wide variety of crop and native plant seeds; the materials should be biodegradable, and the manufacturing process should be straightforward and accessible.

Taking into consideration the awn topology, the parametric geometries of the tail and coils, and the material's intrinsic properties, we have designed and fabricated (Fig. 1a) a three-tailed seed carrier platform from wood veneer, a stiff biomass. The platform (Fig. 1b) consists of: a three-tailed configuration to increase the initial drilling success; a hygromorphic coiling body with variable geometrical factors that are optimized on the basis of both manufacturability and required thrust force and actuation amplitude; and a varying tip and overall sizes to accommodate different payloads. The three-tailed seed carrier performs significantly better than the *Erodium guinum* seed (Fig. 1c) and the hygroscopic seeds of four other natural species under the same testing conditions (Supplementary Note 1), with more noticeable advantages on relatively flat soil (Fig. 1c). The engineering solution we present here is inspired by nature, yet provides flexibility for tailoring (Fig. 1d), according to the specific terrains and payloads including different seeds, symbiotic species and beneficial nematodes. Figure 1e illustrates an example of a carrier containing both vegetable seeds and mycorrhizal fungi as symbiotic biofertilizers[25] in the same tip for aerial

[1]Morphing Matter Lab, Human-Computer Interaction Institute, Carnegie Mellon University, Pittsburgh, PA, USA. [2]Accenture Labs, San Francisco, CA, USA. [3]College of Computer Science and Technology, Zhejiang University, Hangzhou, China. [4]School of Art and Archeology, Zhejiang University City College, Hangzhou, China. [5]Materials Science and Engineering, University of Pennsylvania, Philadelphia, PA, USA. [6]Department of Mechanical and Aerospace Engineering, Syracuse University, Syracuse, NY, USA. [7]BioInspired Syracuse, Syracuse University, Syracuse, NY, USA. ✉e-mail: guanyun@zju.edu.cn; shuyang@seas.upenn.edu; tzhang48@syr.edu; liningy@andrew.cmu.edu

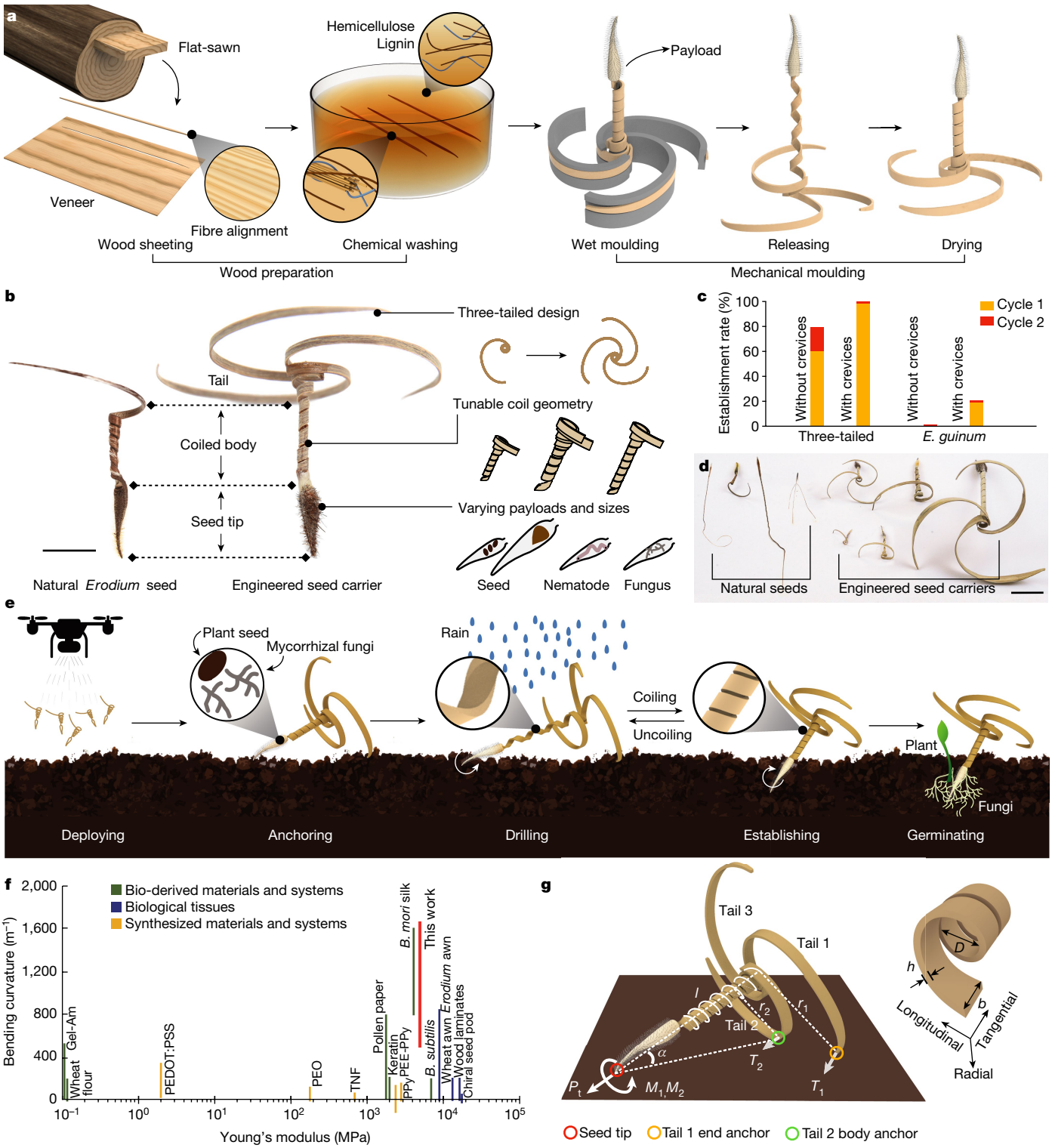

Fig. 1 | Bioinspired design of the autonomous self-drilling seed carrier. **a**, The processing steps to create wood-based hygromorphic actuators with a large initial curvature. **b**, The natural *E. guinum* seed that serves as the design inspiration, and our design concepts of the autonomous self-drilling seeding carrier with customized awn and tailored payloads. Scale bar, 10 mm. **c**, Our engineered three-tailed seed carrier has 80% higher establishment rates than the *Erodium* seed in the controlled self-drilling test (see Methods). $n = 10$ seeds of each type. **d**, Engineered and natural seed carriers of various sizes and geometries (Supplementary Table 1). Scale bar, 20 mm. **e**, A possible application showing a three-tailed carrier delivering vegetable seeds alongside mycorrhizal fungi as symbiotic biofertilizers. **f**, Comparison of our actuator in elastic modulus and bending curvature with typical biological and engineered actuators and materials that exhibit hydration-induced reversible deformation behaviours (see Supplementary Table 2 for additional references and values). Gel-Am, gelatin–amyloid; PEDOT:PSS, poly(3,4-ethylenedioxythiophene):poly (styrene sulfonate); PEO, polyethylene oxide; TNF, titanium oxide nano-capillary forest; PEE-PPy, pentaerythritol ethoxylate-polypyrol; PPy, polypyrol; *B. mori* silk, *Bombyx mori* silk. *B. subtilis*, *Bacillus subtilis*. **g**, Three-tailed design considerations. Successful drilling relies on the effective vertical thrust force (P_t) and torque (M_1, M_2) that are determined by the moisture-driven mechanics coupled with the wood and the coil's dimensional factors, including the thickness (h), width (b), diameter (D) and the coil's active length (l) and tail configurations.

deployment, increasing the potential soil coverage and survival rates. Self-drilling is enabled by natural rain outdoors, achieving a 66 ± 16% success rate of anchoring (30% tip burial, $n = 136$).

Compared to existing biological and synthetic hygromorphic actuators (Fig. 1f), our system has a maximum bending curvature of 1,854 m^{-1} that is 45 times larger than that of reported wood-based bending actuators[15–17], and has a fairly large elastic modulus (about 4.9 GPa).

Design considerations

To effectively drill into the soil, the seed carrier must generate sufficient thrust force (P_t) and torque (M_1, M_2), as shown in Fig. 1g. The thrust force can be expressed as $P_t \approx K\delta$, in which δ is the coil axial displacement, and K is the coil spring constant, which is determined by the material's Young's modulus, E, and the geometrical parameters of the coil:

$$K \propto Ebh^3\kappa_c^2/l \quad (1)$$

in which l is the coil length, b is the width, h is the thickness and κ_c is the bending curvature[26]. The torques are expressed as $M_1 = r_1T_1$ and $M_2 = r_2T_2$, in which r_1 and r_2 are the respective distances between tail 1 and tail 2's contact points on the ground to the coil axis, and T_1 and T_2 are the forces applied at the tails' contact points, respectively (Fig. 1g). Additionally, the tip rotational speed ω is known to reduce the drag force and lower the minimum force needed for drilling[27].

Material choices and processing methods

To drill into natural terrain by harvesting ambient moisture fluctuations, the carrier should be hygromorphic with a large K and tightly coiled when dry. Natural wood has well-studied hygromorphic properties[15–18] and is an abundant and environmentally friendly structural material. Compared to other biodegradable, water-responsive materials such as spider silk[28], bacterial spores[29], engineered silk film[30], pollen paper[31] and naturally derived hydrogels[32–35], wood offers superior modulus (about 10 GPa), and processibility on a large scale (centimetre to metre[15,16]; Supplementary Table 2). However, the high modulus also limits wood-based actuators to a small initial curvature (<10 m^{-1}) and a small range of curvature changes (<30 m^{-1})[15–18]. To tackle this challenge, we develop a five-step process that involves both chemical washing and mechanical moulding (Methods), to transform the bulk wood into a tight hygromorphic coiling actuator.

First, white oak lumbers are flat-sawn cut (Fig. 1a) for veneer processing. After comparing six common wood types, which have relatively uniform fibre alignment, we chose white oak, as it has the largest actuation range and exhibits good moulding quality without material failure (Methods). White oak also has a relatively high tensile modulus (about 13.5 GPa) among common wood types (Supplementary Table 3). The subsequent chemical washing step[36–38] in a boiling bath of sodium hydroxide and sodium sulfite partially removes lignin, thus reducing the strength of the wood[36] and making the sheet compliant for mechanical moulding[39]. To balance the requirements of high stiffness for self-drilling, compliances for wet-moulding, as well as the hygromorphic actuation speed and reversibility (Methods), we prepare our samples from 10-min chemically washed veneer that is 0.5 mm thick. Similar chemical washing and moulding processes have mostly been used to create environmentally durable wood[39], with one exceptional attempt[24] to engineer hygromorphic actuators. However, without understanding its mechanism of curvature formation and the analysis of both geometrical and mechanical factors that affect the actuation behaviours, it failed to reveal a reliable design guideline or an optimized manufacturing pipeline to yield specific shapes and functions efficiently.

Curvature and actuation mechanism

To reveal the underlying mechanisms of curvature formation and actuation, we first analyse the deformation behaviours of the bending actuators, made from the three-step moulding process (Fig. 2a–d). The wet-moulding and wet-releasing steps set an initial bending curvature, and further drying increases this curvature. The curvature of the wood veneer in the wet state after the release, κ_w, increases with its thickness, h, from a large-diameter mould but decreases with h from a small-diameter mould (Fig. 2e). We reason that κ_w is determined by the plastic deformation accumulated in the moulding process. If we assume that plastic deformation occurs only under compression on the inner side of the veneer and adopt a simplified plastic model with an ideal plastic region followed by a stiffening region[39,40] (Fig. 2f), the nonlinear trend can be explained by a beam bending model with asymmetric plastic materials (Methods). All experimental data collapse onto two master curves (Fig. 2g), determined by a dimensionless variable, κh, in which κ is the bending curvature with respect to the neutral axis of the wood sheet during moulding. The grey master curve describes the increase in dimensionless curvature, κ_w/κ, due to the accumulation of the plastic strain. The decrease of κ_w/κ in the black master curve can be attributed to the fact that the compression strain in the stiffening regime becomes reversible.

As the wet-released wood veneer undergoes drying, the bending curvature further increases, eventually reaching a maximum value, κ_d (Fig. 2d). The curvatures in the wet and dry states are proportional, such that $\frac{\kappa_d}{\kappa_w} \approx 2.0$ (Fig. 2h). The increase of κ_d in the drying step can be attributed to: the decrease along the thickness, h, direction; and the gradient shrinkage in the longitudinal direction of the veneer. First, h decreases by 20% during dehydration. On the basis of the reversible actuation in multiple dehydration and hydration cycles (Fig. 2i), we assume that the plastic strain is independent of the moisture-driven shrinkage. We show that a reduction in thickness will lead to an increase in the bending curvature, such that $\frac{\kappa_d}{\kappa_w} = \frac{h}{h'}$, in which h' is the thickness of the dry wood veneer (Methods).

However, the decrease in thickness cannot account for the total increase in κ_d. Our experiments show that the longitudinal shrinkage exhibits a clear gradient across the thickness direction: the inner edge shrinks by 5% to 23%, whereas the outer edge expands by 1% to 4% (Fig. 2j). Scanning electron microscopy images (Fig. 2k,l and Supplementary Note 2) show that the cells towards the inner side have a larger microfibril angle (MFA) μ_{inner} range (23 ± 7°), whereas those towards the outer side have a smaller MFA μ_{outer} (9 ± 2°). By contrast, in the case of chemically washed yet unmoulded wood veneers, the MFA is relatively uniform and small (9 ± 2°, Extended Data Fig. 1b) across the thickness, indicating that the increased μ_{inner} can be attributed to the stress-induced microfibril disorientation[41] during the moulding and drying process. As an increase in MFA can contribute to an increase in longitudinal shrinkage during drying[42], the differences between the MFAs induced by our moulding process provide a qualitative explanation of the measured larger shrinkage ratio of the inner side than that of the outer side. This in combination with the changes in thickness contributes to the dry curvature, κ_d, as well as the reversible curvature changes during actuation cycles, as illustrated in Fig. 2m. This is experimentally validated in three consecutive actuation cycles with a 98% and 85% recovery of the initial curvatures for bending and coiling actuators, respectively (Extended Data Fig. 2).

Combining the effects of the shrinkages along the radial (across the thickness) and longitudinal directions, the dry curvature can be expressed as $\frac{\kappa_d}{\kappa_w} = \frac{h}{h'}(1+\beta)$, in which β is an empirical parameter that describes the coupling between the mechanical strain and shrinkage (Methods). The experimental data can be captured reasonably well in Fig. 2h with $\beta = 0.6$. Note that the cellular size differences are not considered in our analysis. In practice, we try to optimize our manufacturing process to minimize the impact of the heterogeneity in wood samples (Supplementary Note 3).

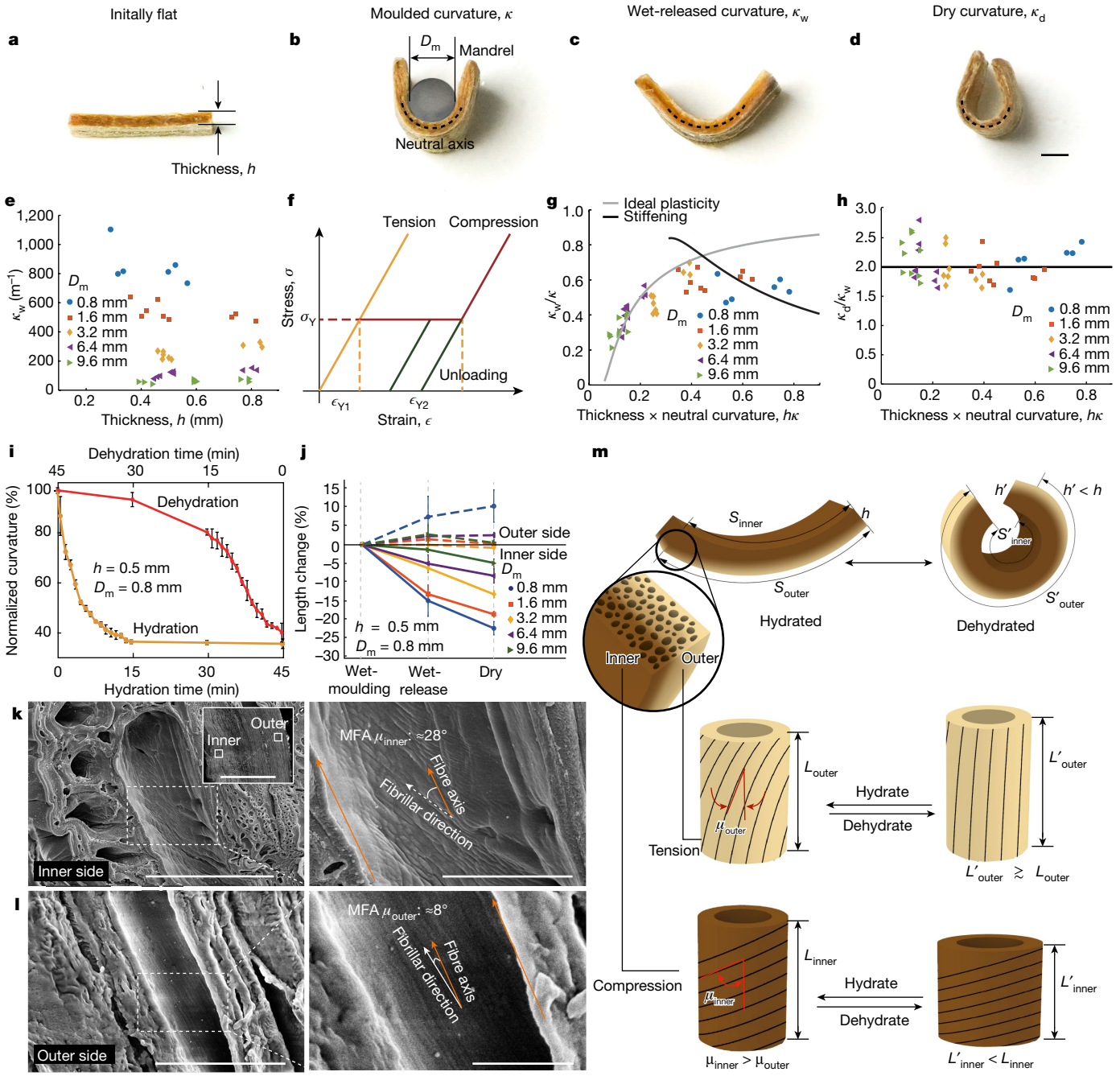

Fig. 2 | The curvature formation mechanism and hygromorphic actuation. **a**–**d**, The curvature changes for ≈0.05-mm-thick flat wood veneer (**a**) evolve from the as-moulded state (**b**) to the wet-released state (**c**) to the dry state (**d**). Scale bar, 1 mm. **e**, The curvature of samples with different thicknesses in the wet-released state after being moulded and released from mandrels of varying diameters. **f**, The simplified plastic model with an ideal plastic region ($\epsilon_{Y_1} \le \epsilon \le \epsilon_{Y_2}$), followed by a stiffening region ($\epsilon_{Y_2} < \epsilon$). **g**, The normalized curvature in the wet state after release. **h**, The normalized curvature in the dry state. For **e**–**h**, each test group contains three samples with an initial thickness of 0.36 ± 0.00 mm, 0.51 ± 0.03 mm and 0.73 ± 0.01 mm, respectively. **i**, Curvature changes of bending samples. Data are means ± s.d. $n = 3$ triggering cycles. The lines provide visual guidance by connecting data points. **j**, Comparison of length changes of the inner and outer side of the wood strips, moulded with mandrels of varying diameters. Data are means ± s.d. $n = 3$ samples. **k**,**l**, A set of representative scanning electron micrographs of the wood strip after moulding and drying: the deformed cells towards the inner side tend to have larger MFAs than the cells towards the outer side with relatively smooth cell walls. Scale bars, 30 μm (**k**, left), 10 μm (**k**, right; **l**, left), 5 μm (**l**, right) and 400 μm (**k**, inset). **m**, Illustrations of the curvature formation and actuation mechanisms.

Geometrical parameters

The topology of the three-tailed design helps secure an initial angle (α) between the tip and the ground (Fig. 1g), which is critical to generating effective torque and thrust force to increase the chance of successful drilling. When dropped on the soil 30 times from 0.3 m above the surface in an indoor controlled test, *Erodium* seeds have an 80% chance of landing flat ($\alpha = 0$), whereas the three-tailed carrier has a 90% chance of landing at an angle between 25° to 30° (Supplementary Video 2). Drone deployment of the three-tailed seed carriers (Extended Data Fig. 3) from 5 to 6 m above ground results in a 90% success rate of landing at a beneficial initial angle. A subsequent self-drilling test shows

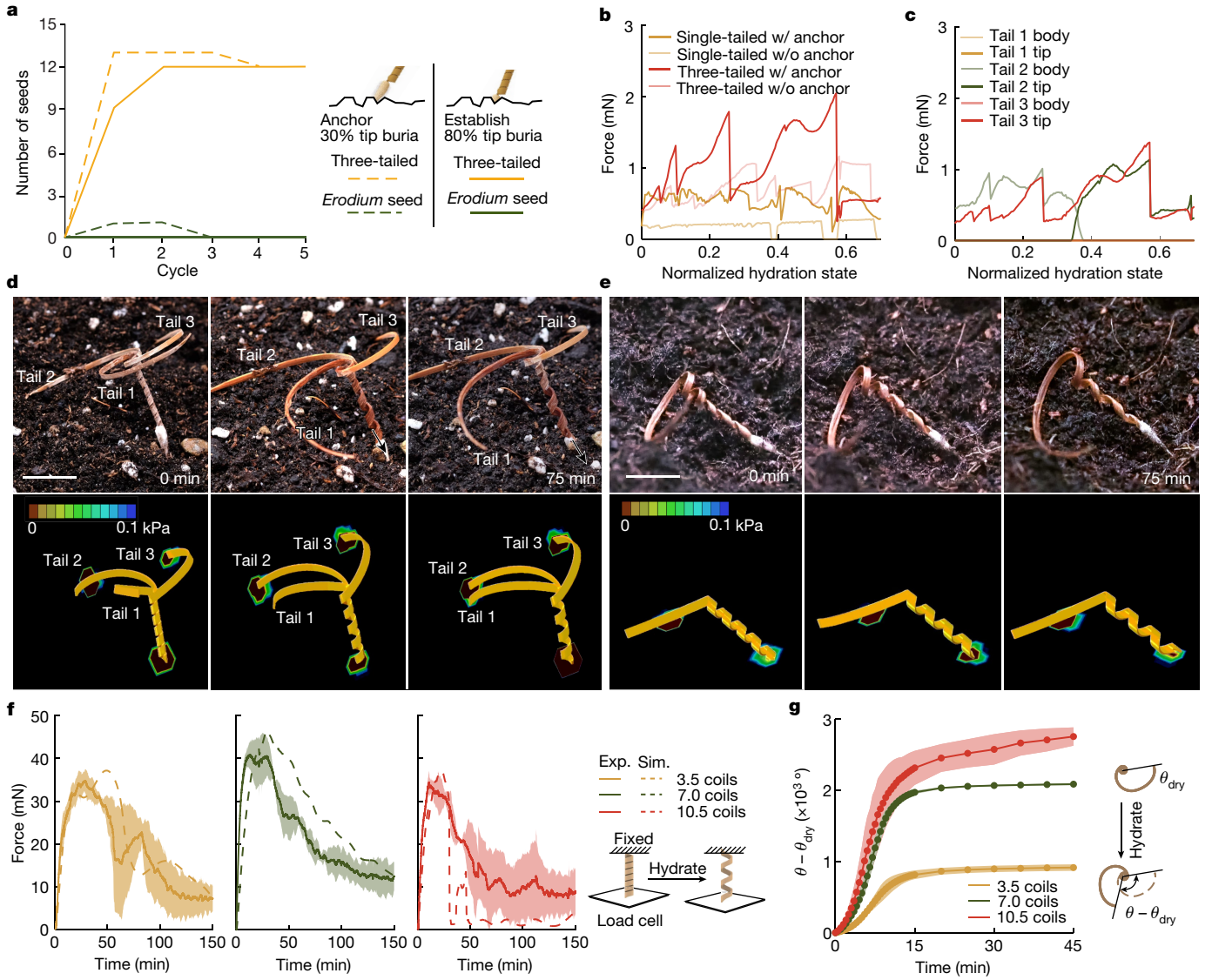

Fig. 3 | Geometrical parameters of the seed carrier design. a, Comparison of drilling success between the three-tailed and *Erodium* seeds on flat soil in five cycles (Methods). $n = 15$ of each type. **b**, Comparison of simulated thrust force between the seed tip and the ground from the three-tailed and the single-tailed designs, as a function of the normalized hydration state (Methods) that maps the transition from the dry state (0) to the wet state (1). w/, with; w/o, without. **c**, Simulation results of the dynamic forces generated by multiple tails of the three-tailed design. **d**,**e**, Experimental and simulation snapshots of the three-tailed (**d**) versus the single-tailed (**e**) seed carriers, during the first hydration cycle triggered by natural rain. For the three-tailed design shown in **d**, the body of tail 2 and the tip of tail 3 generate forces initially, and then the tips of both tail 1 and 2 start to generate larger forces as the tails get more hydrated. By contrast, the force stays relatively constant and small for the single-tailed design in **e**. The colour bar represents the contact pressure, which is greater than 0.1 kPa. The small upper bond is to help visualizations of the contact regions. Scale bars, 10 mm. **f**, Experiments (Exp.) and simulation (Sim.) of peak extension forces of coiling actuators with different coiling numbers. Data are means ± s.d., $n = 3$ of each coiling number. Schematic shows the setup of the measurements, where one end of the coils is fixed during hydration, and the sample is sandwiched between the fixed end and the load cell. **g**, Rotational range and speed of coiling actuators. Data are means ± s.d., $n = 3$ of each coiling number. Schematic shows the change in rotational range being measured as the sample is hydrated.

that four out of five three-tailed seed carriers successfully established tip burial after two hydration–dehydration cycles, whereas none of the single-tailed carriers achieved this after five cycles (Fig. 3a, Supplementary Video 3 and Methods). We conduct further finite-element simulations to qualitatively predict the coiling actuator performance taking into consideration the frictional interaction between the seed carriers and soil, and the potential anchoring effect (Methods). As seen in Fig. 3b, the three-tailed design generates a much larger thrust force than the single-tailed design. Figure 3c shows that the body of tail 2 and the tip of tail 3 of the three-tailed design anchor initially, and then both tips of tail 2 and 3 start anchoring on the ground to generate larger forces as the tails become more hydrated. For both designs, an anchoring seed tip can significantly increase the thrust force; the representative dynamic hydration process in both experiments and simulations is shown in Fig. 3d,e and Supplementary Video 4.

To quantify how the length of the active coiled body, l, affects the extension force, P_e, we measure P_e with varying total numbers of coils. Among the coiling samples tested in Fig. 3f and Supplementary Note 4, the 3.5 coils with an initial thickness of 0.74 ± 0.06 mm provided the largest peak extension force of 55.18 ± 6.82 mN, which is about 34% larger than that of the *Erodium* seed coils (36.57 ± 2.44 mN).

Although increasing the total number of coils increases the tip rotational speed ω (Fig. 3g), which will reduce the drag force between the tip and the soil to facilitate drilling[27], it also decreases the generated

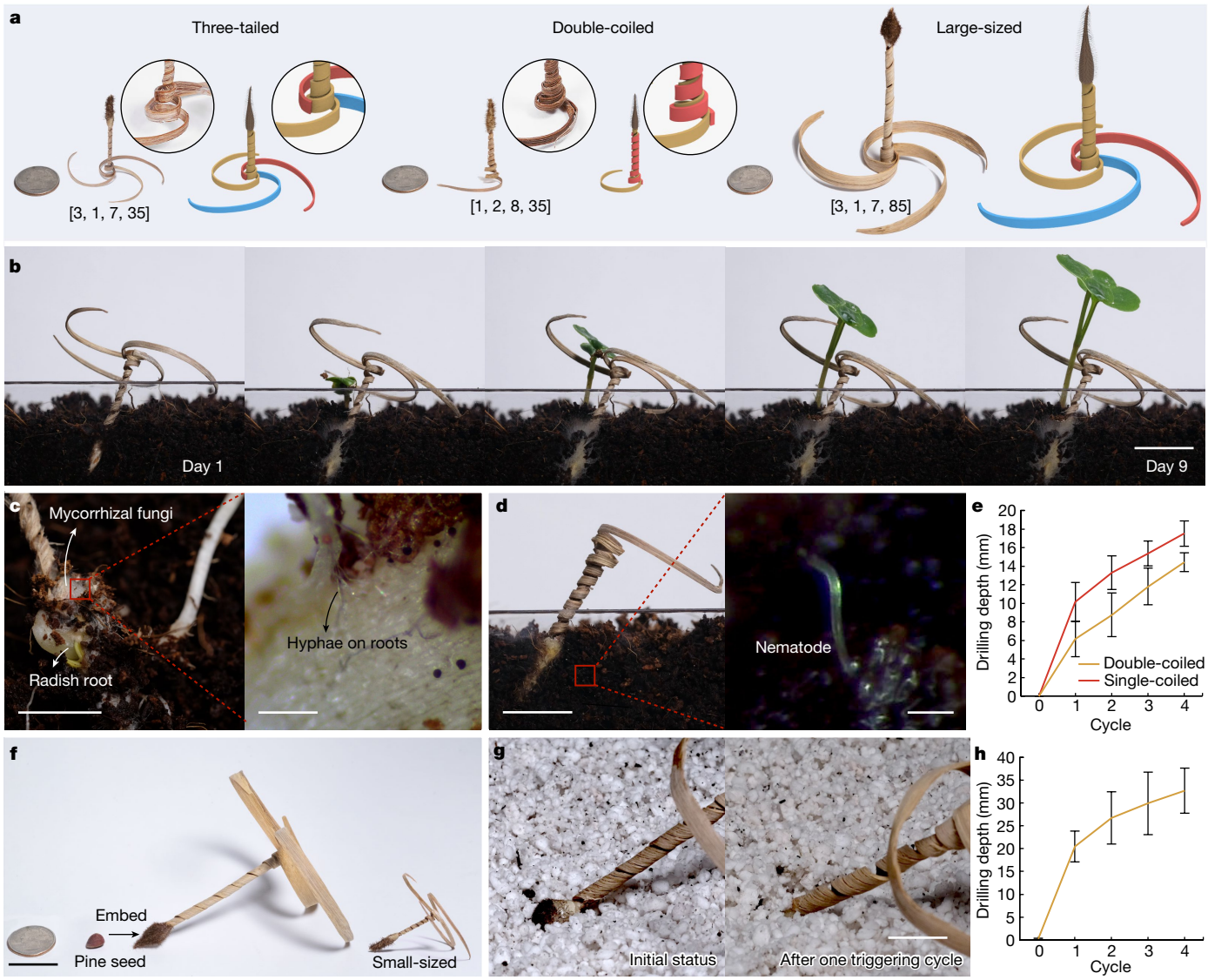

Fig. 4 | Tailored designs of self-drilling carriers. a, Three different engineered seed carrier designs with different size, coil and tail variations. The identifying numbers beneath each case indicate, respectively: the total number of tails; the total layers of the coiled body; the total numbers of coils; and the total body length in millimetres. **b**, The germination process of a three-tailed seed carrier with embedded symbiotic species: cherry belle radish seeds and mycorrhizal fungi. Scale bar, 10 mm. **c**, The symbiotic growth of radish seeds and mycorrhizal fungi. Scale bars, 5 mm (left) and 10 µm (right). **d**, Burial state 9 days after delivery of the beneficial nematodes, *S. carpocapsae*, by a double-coiled seed carrier. Scale bars, 10 mm (left) and 200 µm (right). **e**, Comparison of the self-drilling depth between the double-coiled and single-coiled seed carriers. Data are means ± s.d., $n = 10$ for each type. **f**, A large-sized seed carrier is designed to carry whitebark pine seed for reforestation. Scale bar, 24 mm. **g**, The successful drilling of the large-sized seed carrier with a whitebark pine seed after the first triggering cycle. Scale bar, 10 mm. **h**, Drilling depth of large-sized seed carrier with a body length of about 302 mm. Data are means ± s.d., $n = 8$ anchored ones from a total of 10 samples. More details for the tests in **b**–**h** are included in the Methods.

extension force, P_e (Fig. 3f). This motivates us to use seven coils to design the body for a balanced thrust force and rotational speed.

Tailored seed carrier designs

The geometric-based designs allow us to tailor the self-burial seed carriers for different terrain conditions and payloads (Fig. 4a and Supplementary Video 5). The process to integrate different payloads is shown in Extended Data Fig. 4 and Supplementary Video 6, and the drilling test conditions are described in the Methods. Two symbiotic species—two cherry belle radish seeds and 1 mg of mycorrhizal fungi as a soil nutrient—embedded within one tip were successfully deployed in fibre soil after four triggering cycles (Methods). After 9 days, the seeds germinated and the fungi was visible near the plant roots under a light microscope (Fig. 4b,c and Supplementary Video 7).

We then tested the delivery of beneficial nematodes, *Steinernema carpocapsae*, which improve plant health[43] but require deeper burial, as nematodes prefer to grow in a dark environment[44]. To increase the drilling depth, we engineered a double-coiled seed carrier (Fig. 4d), which achieved a deeper burial (16.5–18 mm) than the single-coiled carrier after four triggering cycles (Fig. 4e and Extended Data Fig. 5). We tracked the delivery of nematodes from our seed carriers to the surrounding soils over a period of 9 days in a controlled test (Methods). Living nematodes could be identified from the second day, and the total number continued to increase, reaching a peak of 34,760 ± 6,525 per kilogram of soil on day 4 (Extended Data Fig. 6 and Supplementary Video 8).

To carry relatively large whitebark pine seeds (about 11 mm in length and about 72 mg), we fabricated a large-sized seed carrier (302.7 mm long; Fig. 4f), which showed successful self-burial on a perlite bed in the first triggering cycle (Fig. 4g,h).

Drilling test under natural stimuli

We conducted five outdoor drilling experiments with 136 three-tailed seed carriers in two geographical locations over two springs (Supplementary Table 4 and Methods). Compared to laboratory tests, the drilling success rate decreased, with an anchoring rate of 66 ± 16% and an establishment rate of 39 ± 13%. As expected, the drilling success is significantly affected by the varying and unpredictable weather conditions. For example, in drilling test 1 (Extended Data Fig. 7a), two periods of intermittent, light rain on the first day triggered a 95% anchoring rate, yet a heavy rainstorm on the second day dislodged 56% of the previously anchored seed carriers. In drilling test 3, sunlight after the rain was found to promote further seed establishment with a 15% increase (Extended Data Fig. 7b).

Heavy rain can also damage the seed tips, preventing seed carriers from further drilling, even though the coiled body and tails could later recover from the flood and further functionally coil and uncoil. We expect that further optimization of the seed tips[24] could improve their resilience to harsh environments and hostile climate effects, such as extreme flooding or drought. The influence of soil types and surface roughness needs more quantification in the future, to tailor our designs and increase the success rate.

Temperature seems to affect the drilling performance. A higher average temperature in the field tests resulted in a higher (33.5%) establishment rate. In a controlled test, the extension force of the seven coils decreased from 42.47 ± 4.48 mN to 31.45 ± 2.63 mN when the temperature dropped from about 30 °C to about 18 °C (Supplementary Note 5).

To measure the germination rate, we tracked the seed carriers in drilling tests 1–3 and 5 (Supplementary Note 5 and Supplementary Video 9). After 15 days, we identified 75 remaining seed carriers with embedded arugula seeds. Of those, 43 seeds anchored and had a 61% germination rate, whereas the remaining 32 dislodged or unanchored seeds had a 12% germinate rate. A consecutive germination test of 400 seed carriers in the later summer season indicated a consistent advantage of the buried seeds over the unburied ones, yet with an overall lower germination rate than the tests conducted in earlier seasons (Supplementary Note 5).

Conclusion

We uncover the design principle that turns wood veneer into stiff and biodegradable hygromorphic actuators with an extremely large bending curvature (1,854 m^{-1}). We then design three-tailed seed carriers that can self-drill into the ground in response to moisture fluctuations in the environment, with a drilling success rate superior to that of their natural counterparts, such as *Erodium* seeds. Our engineered carrier can be tailored for quick deployment of seeds, microorganisms and other soil nutrients through aerial delivery, with promising implications for agriculture, reforestation and natural conservation in environmentally degraded regions. The design principle along with customized moulding can be used to create wood-based hygromorphic actuators with versatile shapes and functions, including coiling, bending, linear or radial contraction, twisting and folding for broad applications, including sustainable robotics, as well as adaptive structures and environmental monitoring under climate changes. For example, hygromorphic actuators have been used to engineer evaporation-driven engines[45], self-flipping sheets for energy harvesting[46] and robots that self-crawl according to moisture gradients[47] and environmental sensing[24]. Biomass such as wood offers an alternative to synthetic materials for the engineered hygromorphic actuators with superior performance. Furthermore, combining our method with other wood processing methods including lamination[15], impregnation[48] and densification[37] may generate multi-functional wood structures (for example, programmable response rate, increased energy density and multi-stimuli responsiveness) and new scientific insights as well. For the purpose of scaling up, a further optimization of the manufacturing process and life cycle analysis[39] will be needed.

Online content

Any methods, additional references, Nature Portfolio reporting summaries, source data, extended data, supplementary information, acknowledgements, peer review information; details of author contributions and competing interests; and statements of data and code availability are available at https://doi.org/10.1038/s41586-022-05656-3.

1. Fisher, K. A., Momen, B. & Kratochvil, R. J. Is broadcasting seed an effective winter cover crop planting method? *Agron. J.* **103**, 472–478 (2011).
2. Ball, B. C. Cereal production with broadcast seed and reduced tillage: a review of recent experimental and farming experience. *J. Agric. Eng. Res.* **35**, 71–95 (1986).
3. Kelly, L. T. et al. Fire and biodiversity in the Anthropocene. *Science* **370**, eabb0355 (2020).
4. Keane, R. E. Managing wildfire for whitebark pine ecosystem restoration in western North America. *Forests* **9**, 648 (2018).
5. Xiao, X. et al. Aerial seeding: an effective forest restoration method in highly degraded forest landscapes of sub-tropic regions. *Forests* **6**, 1748–1762 (2015).
6. Monsen, S. B., Stevens, R. & Shaw, N. L. *Restoring Western Ranges and Wildlands, vol. 1.* (US Department of Agriculture, Forest Service, Rocky Mountain Research Station, 2004).
7. Ranwell, D. S. in *Geology and Engineering* (Ed. Cronin, L. E.) 471–483 (Elsevier, 1975).
8. Collins, B. A. & Fowler, D. B. A comparison of aerial and conventional methods for seeding winter wheat. *Soils and Crops Workshop* (University of Saskatchewan, 1989).
9. Keisling, T. C., Dillon, C. R., Oxner, M. D. & Counce, P. A. An economic and agronomic evaluation of selected wheat planting methods in Arkansas. In *Proc. Southern Conservation Tillage Conference* 156–158 (1997).
10. Stamp, N. E. Self-burial behaviour of *Erodium cicutarium* seeds. *J. Ecol.* **72**, 611–620 (1984).
11. Ha, J. et al. Hygroresponsive coiling of seed awns and soft actuators. *Extreme Mech. Lett.* **38**, 100746 (2020).
12. Almeida, A. P. C. et al. Reversible water driven chirality inversion in cellulose-based helices isolated from *Erodium* awns. *Soft Matter* **15**, 2838–2847 (2019).
13. Abraham, Y. et al. Tilted cellulose arrangement as a novel mechanism for hygroscopic coiling in the stork's bill awn. *J. R. Soc. Interface* **9**, 640–647 (2012).
14. Evangelista, D., Hotton, S. & Dumais, J. The mechanics of explosive dispersal and self-burial in the seeds of the filaree, *Erodium cicutarium* (Geraniaceae). *J. Exp. Biol.* **214**, 521–529 (2011).
15. Rüggeberg, M. & Burgert, I. Bio-inspired wooden actuators for large scale applications. *PLoS ONE* **10**, e0120718 (2015).
16. Grönquist, P. et al. Analysis of hygroscopic self-shaping wood at large scale for curved mass timber structures. *Sci. Adv.* **5**, eaax1311 (2019).
17. Holstov, A., Bridgens, B. & Farmer, G. Hygromorphic materials for sustainable responsive architecture. *Constr. Build. Mater.* **98**, 570–582 (2015).
18. Krieg, O. D. in *Advancing Wood Architecture: a Computational Approach* (eds. Achim, M. et al.) 16 (Routledge, Taylor & Francis, 2016).
19. Cavanagh, A. M., Morgan, J. W. & Godfree, R. C. Awn morphology influences dispersal, microsite selection and burial of Australian native grass diaspores. *Front. Ecol. Evol.* **8**, 581967 (2020).
20. Tothill, J. C. Soil temperatures and seed burial in relation to the performance of *Heteropogon contortus* and *Themeda australis* in burnt native woodland pastures in eastern Queensland. *Aust. J. Bot.* **17**, 269–275 (1969).
21. Rice, K. J. Responses of *Erodium* to varying microsites: the role of germination cueing. *Ecology* **66**, 1651–1657 (1985).
22. Garnier, L. K. M. & Dajoz, I. Evolutionary significance of awn length variation in a clonal grass of fire-prone savannas. *Ecology* **82**, 1720–1733 (2001).
23. Keane, R. E. & Parsons, R. A. *Management Guide to Ecosystem Restoration Treatments: Whitebark Pine Forests of the Northern Rocky Mountains, U.S.A.* 133 (US Department of Agriculture, Forest Service, Rocky Mountain Research Station, 2010).
24. Luo, D., Gu, J., Qin, F., Wang, G. & Yao, L. E-seed: shape-changing interfaces that self drill. In *Proc. 33rd Annual ACM Symposium on User Interface Software and Technology* 45–57 (Association for Computing Machinery, 2020).
25. Igiehon, N. O. & Babalola, O. O. Biofertilizers and sustainable agriculture: exploring arbuscular mycorrhizal fungi. *Appl. Microbiol. Biotechnol.* **101**, 4871–4881 (2017).
26. Jung, W., Kim, W. & Kim, H.-Y. Self-burial mechanics of hygroscopically responsive awns. *Integr. Comp. Biol.* **54**, 1034–1042 (2014).
27. Jung, W., Choi, S. M., Kim, W. & Kim, H.-Y. Reduction of granular drag inspired by self-burrowing rotary seeds. *Phys. Fluids* **29**, 041702 (2017).
28. Agnarsson, I., Dhinojwala, A., Sahni, V. & Blackledge, T. A. Spider silk as a novel high performance biomimetic muscle driven by humidity. *J. Exp. Biol.* **212**, 1990–1994 (2009).
29. Chen, X., Mahadevan, L., Driks, A. & Sahin, O. *Bacillus* spores as building blocks for stimuli-responsive materials and nanogenerators. *Nat. Nanotechnol.* **9**, 137–141 (2014).
30. Park, Y. et al. β-Sheet nanocrystals dictate water responsiveness of *Bombyx mori* silk. *Macromol. Rapid Commun.* **41**, 1900612 (2020).
31. Zhao, Z. et al. Digital printing of shape-morphing natural materials. *Proc. Natl Acad. Sci. USA* **118**, e2113715118 (2021).
32. Shintake, J., Sonar, H., Piskarev, E., Paik, J. & Floreano, D. Soft pneumatic gelatin actuator for edible robotics. In *2017 IEEE/RSJ International Conference on Intelligent Robots and Systems (IROS)* 6221–6226 (IEEE, 2017).
33. He, Q., Huang, Y. & Wang, S. Hofmeister effect-assisted one step fabrication of ductile and strong gelatin hydrogels. *Adv. Funct. Mater.* **28**, 1705069 (2018).
34. Baumgartner, M. et al. Resilient yet entirely degradable gelatin-based biogels for soft robots and electronics. *Nat. Mater.* **19**, 1102–1109 (2020).

35. Zhao, D. et al. High-strength and high-toughness double-cross-linked cellulose hydrogels: a new strategy using sequential chemical and physical cross-linking. *Adv. Funct. Mater.* **26**, 6279–6287 (2016).
36. Song, J. et al. Processing bulk natural wood into a high-performance structural material. *Nature* **554**, 224–228 (2018).
37. Frey, M. et al. Delignified and densified cellulose bulk materials with excellent tensile properties for sustainable engineering. *ACS Appl. Mater. Interfaces* **10**, 5030–5037 (2018).
38. Frey, M. et al. Tunable wood by reversible interlocking and bioinspired mechanical gradients. *Adv. Sci.* **6**, 1802190 (2019).
39. Xiao, S. et al. Lightweight, strong, moldable wood via cell wall engineering as a sustainable structural material. *Science* **374**, 465–471 (2021).
40. Holmberg, S., Persson, K. & Petersson, H. Nonlinear mechanical behaviour and analysis of wood and fibre materials. *Comput. Struct.* **72**, 459–480 (1999).
41. Báder, M., Németh, R. & Konnerth, J. Micromechanical properties of longitudinally compressed wood. *Eur. J. Wood Wood Prod.* **77**, 341–351 (2019).
42. Donaldson, L. Microfibril angle: measurement, variation and relationships – a review. *IAWA J.* **29**, 345–386 (2008).
43. Goodrich-Blair, H. They've got a ticket to ride: *Xenorhabdus nematophila–Steinernema carpocapsae* symbiosis. *Curr. Opin. Microbiol.* **10**, 225–230 (2007).
44. Gaugler, R. & Boush, G. M. Effects of ultraviolet radiation and sunlight on the entomogenous nematode, *Neoaplectana carpocapsae*. *J. Invertebr. Pathol.* **32**, 291–296 (1978).
45. Chen, X. et al. Scaling up nanoscale water-driven energy conversion into evaporation-driven engines and generators. *Nat. Commun.* **6**, 7346 (2015).
46. Park, Y. & Chen, X. Water-responsive materials for sustainable energy applications. *J. Mater. Chem. A* **8**, 15227–15244 (2020).
47. Shin, B. et al. Hygrobot: a self-locomotive ratcheted actuator powered by environmental humidity. *Sci. Robot.* **3**, eaar2629 (2018).
48. Wen, M.-Y., Kang, C.-W. & Park, H.-J. Impregnation and mechanical properties of three softwoods treated with a new fire retardant chemical. *J. Wood Sci.* **60**, 367–375 (2014).

Methods

Fabrication

The five-step approach (Extended Data Fig. 4) is summarized briefly here, and the details are provided in Supplementary Note 6. A 3-cm-thick white oak (*Quercus alba*) lumber is flat-sawn into a block, which is then processed into wood veneers with a target thickness. The obtained wood strips are immersed in a boiling aqueous solution of 2.5 M sodium hydroxide (NaOH, Innovating Science, laboratory-grade) and 0.4 M sodium sulfite (Na_2SO_3, LabChem, ACS grade) for 10 min, followed by rinsing in boiling water with gentle agitation three times until the water is clear. To make the coiling actuators, the chemically washed veneer strips are pat-dried on a paper towel and sat in the open air for 6 min before being moulded tightly on a three-dimensionally printed mould (by Formlabs 3). The moulded wood veneer is released from the mould while still wet, and dried at room temperature for 12 h.

Choices of wood types

To identify a suitable wood type as an actuator, we needed to consider the balance between stiffness and mouldability. To maximize the thrust force, we preferred stiffer wood. However, to produce tight coils, we needed the wood to be readily mouldable after chemical wash in the wet state. We also needed to choose wood that has a uniform fibre alignment, so we could laser cut a strip with a high aspect ratio along the fibre direction, to optimize its bending stiffness and integrity during the moulding process (certain types of wood can easily be torn apart between fibres).

We identified six types of wood that have relatively well-aligned fibres to evaluate their mouldability and actuation range. We were not able to mould yellowheart and bamboo into bending samples successfully. White oak has the largest initial dry curvature and actuation range among the four wood types that were successfully moulded (Extended Data Fig. 8a). Using the same coiling mould, we tried to mould the seed carrier. Consistent with the bending actuator test, bamboo and yellowheart fractured during the moulding process, whereas the others did not show visible fractures (Extended Data Fig. 8b). As different types of wood may behave differently under various chemical washing conditions (for example, chemical mixing ratio and washing duration), further quantitative experiments need to be conducted to optimize the chemical treatment, if we intend to carry out a successful moulding process with a wood type other than white oak. Further guidelines for choosing wood types are provided in Supplementary Note 7.

Optimization of the chemical washing and moulding parameters

We conducted experiments to optimize the processing parameters. We compared the actuation amplitude of bending samples chemically washed for 5 min, 10 min and 15 min, respectively. The samples washed for 10 min resulted in the largest actuation range (Extended Data Fig. 8c). We further tested different mandrel diameters and sample thicknesses. With the same chemical washing duration of 10 min, the moulding started to fail as the wood veneer exceeded 0.8 mm in thickness. In addition, mandrels with smaller diameters induced more fractures on the tensile side of the wood strip (Extended Data Fig. 8d).

Peak force measurement

The extension forces of the coils described in Fig. 3f and Supplementary Note 4 were measured in a customized chamber with controlled temperature and relative humidity. A load cell is configured to measuring the extension forces. Supplementary Note 4 provides further details regarding the setup.

Bending curvature measurement

We measured the bending angles of both bending (Fig. 2a–j) and coiling (Fig. 3g) actuators in multiple cycles to understand the actuation amplitude, speed and recovery. Each actuator underwent multiple hydration and dehydration cycles. The hydration processes were conducted in a water tank; the water in the tank was kept at 25 °C. During the dehydration processes, the samples were taken out of the water tank and kept at 25 °C with relative humidity within the range of 30–40%. The images used in the analyses were taken by a camera (XT-1, Fujifilm) with a macro lens (XF 60mm *f*/2.4 R, Fujifilm). Owing to the inherent heterogeneity of wood and the unavoidable inconsistencies induced by the manual laser cutting selection and moulding process, the curvature varied. In the case of samples that were prepared from the wood veneers with relatively consistent thicknesses of 0.51 ± 0.03 mm ($N = 3$), we measured the maximum bending curvature as 1,854.5 ± 96.9 m^{-1} and the actuation range as 1,533.4 ± 56.1 m^{-1} to 596.8 ± 14.2 m^{-1}.

Soil characterization

We measured the surface roughness using a pin method adapted from the literature[49]. Ten pins separated from one another by 1 cm were placed on three sections on each bed. At three randomly chosen locations of the soil surface, we lowered each pin until it touched the substrate. The $\log_{10}$[soil microtopographical variance] (LSMV) was calculated as the variance of the vertical pin heights against a measuring board. For soil compaction, we used a soil penetrometer to measure the unconfined compressive strength of the soil. For granular size, we used a light microscope for the measurement. We list all soil types utilized in Supplementary Table 5, in terms of soil type, granular size, quantified surface topology and compactness.

Self-drilling tests under controlled conditions

The laboratory setting consisted of six misting nozzles and two heated fans mounted above a 50 cm by 50 cm testing area, covered by a single layer of cobblestones underneath a 10 cm layer of perlite (Miracle-Gro). The perlite bed was relatively flat and had a 0.78 LSMV, which is the default soil condition for most indoor drilling tests, unless otherwise specified. For example, artificial crevices of 3 cm deep were introduced for two sets of tests, one included in Fig. 1c and the other in Fig. 4e. In Fig. 1c, in the case of natural *Erodium* seed and engineered single-tailed seed carriers with both single-coiled and double-coiled bodies, the soil was textured with conical crevices to facilitate the drilling process for parallel comparison. In Fig. 4e, crevices were also introduced to compare engineered seed carriers with double-coiled and single-coiled bodies. For other drilling tests, including the three-tailed drilling and large-sized seed drilling tests, no crevices were introduced.

For all the self-drilling tests, multiple cycles of hydration–dehydration were carried out, while the surface temperature of the soil was kept at about 30 °C. For each cycle, hydration lasted for 30 min, followed by a 60-min dehydration cycle. Water was supplied at 70 psi through six brass misting nozzles with an orifice of 0.3 mm (Aootech), and a fanned warm airflow from two electric space heaters (Douhe) was supplied to simulate drying. During hydration, both misting nozzles and fan heaters were on, and during dehydration, only the fan heaters were on.

Indoor germination and incubation

For the indoor germination and incubation experiments in Fig. 4b–d, coconut coir (Mountain Valley Seed Co.) was used as the soil. Four cycles of hydration–dehydration were carried out following the standard protocol developed for the drilling tests under controlled conditions. The self-anchored seed carriers were then left in soil for 9 days, and the soil was kept moist during the experiments at a temperature under 25 °C and at 40% relative humidity.

The germination and microbe-delivery experiments in Fig. 4b,c were conducted with fully biodegradable tips made of flour. An additional 10% wt/wt mycorrhizal fungi (Mikro-myco, mixture of endomycorrhizal fungi (260 colony-forming units (c.f.u.) g^{-1}), ectomycorrhizal fungi (218,000 c.f.u. g^{-1}), *Trichoderma* (750,000 c.f.u. g^{-1}) and *Bacillus* (400,000,000 c.f.u. g^{-1}) was mixed into the flour to make the dough

that was moulded into the seed tip. Two cherry belle radish seeds (Eden Brothers) were embedded in the dough, and the dough was then air dried for 12 h before adding the hairs.

For the microbe-delivery experiment (Fig. 4d), we integrated about 0.05 g of beneficial nematode powder (*Steinernema feltiae*, BioLogic Scanmask) into each seedpod dough by means of further gentle kneading for about 2 min by hand. We conducted an experiment to track nematode delivery for 9 days: we filled 10 separate containers with 20 g of dry coconut coir soil. We then embedded one nematode-loaded seed carrier into each container, which was moistened with 10 ml of water each day. We then extracted and counted the living nematodes from the soil of one container each day using the centrifugal flotation method[50], with sugar water as the extraction fluid, for 9 consecutive days (Extended Data Fig. 6). The same set of tests was repeated three times.

Drone deployment tests

A commercial drone (Phantom 3, DJI) was used to carry a customized box with dividers to store multiple seeds (Extended Data Fig. 3). A magnetic double-side door can be opened with a remote-controlled pulling mechanism once the drone flies to the target height. When multiple seeds are randomly placed together, they entangle. In Supplementary Note 8, we study the entanglement and propose an extendable accordion structure to store and deploy seeds more effectively.

Drilling tests under natural conditions

The field tests were carried out in raised beds (2 m by 1 m) outdoors. The soils were randomly chosen to cover a range of different types (clay, sandy and fibre-rich soils, with their components and roughness characterization provided in Supplementary Table 5). In total, we conducted five rounds of tests in two geographical locations across two spring seasons. The weather conditions, soil used and drilling performance are summarized in Supplementary Table 4. All of the artificial seed carriers were dropped from a height of 30 cm above the surface of the soil, with a separation of at least 10 cm. The seeds were dropped before rainfall, in accordance with the local weather forecast. We kept track of the seeds for the first 2 consecutive days to monitor their drilling performance, and for the following 2 weeks to monitor their germination performance.

Curvature analysis of the bending actuators

Curvature in the wet state just after release. Under scanning electron microscopy (Extended Data Fig. 1a) after moulding, irreversible deformation such as cell wall corrugation and bulges, due to compression, was observed on the inner side but not the outer side. Therefore, we assumed that plastic deformation happens only under compression and we adopted a simplified, plastic model with an ideal plastic region followed by a stiffening region[40,51] (Fig. 2f). The increase of modulus in the stiffening region is due to the contact of the collapsed cell walls[52]. The plastic strain is governed by two critical parameters, ϵ_{Y_1} and ϵ_{Y_2}, defining the boundary of the ideal plastic region and stiffening region, respectively (Fig. 2f). Plastic deformation is accumulated in the inner region of the veneer during the moulding process. On release, the elastically deformed outer layer tends to retract to its original flat shape and thus bends the plastically deformed and curved inner portion of the veneer, resulting in an intrinsic curvature of wood veneers in the wet-released state, κ_w (Fig. 2c), which can be obtained by analysing the competition between the elastic recovery and accumulated plastic deformation (Supplementary Note 9). For wood veneers within the ideal plastic deformation region, κ_w can be expressed as

$$\frac{\kappa_w}{\kappa}=\left(\frac{1}{2}+2\left(-\frac{1}{2}+\sqrt{\frac{2\epsilon_{Y_1}}{\kappa h}}\right)^3-\frac{3}{2}\left(-\frac{1}{2}+\sqrt{\frac{2\epsilon_{Y_1}}{\kappa h}}\right)\right) \tag{1}$$

in which κ is the bending curvature with respect to the neutral axis during the moulding process and given by

$$\kappa=\frac{4(1-\epsilon_{Y_1})^2}{\left(\sqrt{2\epsilon_{Y_1}h+4(R+h)(1-\epsilon_{Y_1})}-\sqrt{2\epsilon_{Y_1}h}\right)^2} \tag{2}$$

Equation (1) shows that wood veneers with different thicknesses and mould curvatures will follow a master curve with $\epsilon_{Y_1}=0.025$, which is validated by our experimental data (Fig. 2g).

For wood veneers within the stiffening deformation region, κ_w can be written as

$$\frac{\kappa_w}{\kappa}=3\frac{(\epsilon_{Y_2}-\epsilon_{Y_1})}{\kappa h}\left(1-4\left(\frac{y_4}{h}\right)^2\right)+\left(4\left(\frac{y_4}{h}\right)^3+2\left(\frac{y_2}{h}\right)^3-6\frac{y_2}{h}\left(\frac{y_4}{h}\right)^2\right) \tag{3}$$

in which $\frac{y_2}{h}=\frac{y_1}{h}+\frac{\epsilon_{Y_1}}{\kappa h}$ and $\frac{y_4}{h}=\frac{y_1}{h}+\frac{\epsilon_{Y_2}}{\kappa h}$ and κ and y_1 are given by

$$\kappa=\frac{\frac{R}{h}(\epsilon_{Y_2}-\epsilon_{Y_1})+1+\sqrt{\left(\frac{R}{h}(\epsilon_{Y_2}-\epsilon_{Y_1})+1\right)^2-4\left(\frac{R}{h}+\frac{1}{2}\right)\left((\epsilon_{Y_2}-\epsilon_{Y_1})-\frac{1}{2}(\epsilon_{Y_2}^2-\epsilon_{Y_1}^2)\right)}}{2R+h} \tag{4}$$

and

$$y_1=(\kappa h+\epsilon_{Y_1}-\epsilon_{Y_2})^{-1}\left(\frac{1}{2\kappa}(\epsilon_{Y_2}^2-\epsilon_{Y_1}^2)-\frac{h}{2}(\epsilon_{Y_2}-\epsilon_{Y_1})\right) \tag{5}$$

Equation (3) also shows that wood veneers with different thickness and mould curvatures will follow a master curve with $\epsilon_{Y_1}=0.025$ and $\epsilon_{Y_2}=0.15$, which is validated by our experimental data (Fig. 2g).

Note that we neglect the modulus reduction and irreversible deformation near the outer layer, due to local fibre damage, to develop a minimum model to explain the curvature formation after the moulding of the wood veneers in the experiments. The current model requires only two fitting parameters, ϵ_{Y_1} and ϵ_{Y_2}, which can capture the nonlinear and non-monotonic bending curvatures in experiments (Fig. 2g). The simplicity and efficiency of the model can serve the purpose of uncovering the key physics governing the bending deformation of the wood veneers.

Curvature in the dry state. Our experiments show that the thickness of the wood veneer undergoes around a 20% decrease during drying ($\frac{h'}{h}=0.8$). We first discuss the thickness shrinkage effect during dying on the curvature change, as shown in Supplementary Fig. 17. In the dry state, the plastic deformation strain can be expressed as

$$\epsilon_p=(y_2'-y')\kappa' \tag{6}$$

in which $y'=\frac{h'}{h}y$ is the scaled coordinate along the thickness direction, y_2' is the new boundary of the plastic region and κ' is is an effective curvature. This mapping indicates that the dry configuration can be effectively obtained by moulding a flat sheet with thickness of h' under the bending curvature of κ'. Therefore, the previous analysis can be directly leveraged to predict the curvature in the dry state as

$$\frac{\kappa_d}{\kappa'}=\left(\frac{1}{2}+2\left(-\frac{1}{2}+\sqrt{\frac{2\epsilon_{Y_1}}{\kappa' h'}}\right)^3-\frac{3}{2}\left(-\frac{1}{2}+\sqrt{\frac{2\epsilon_{Y_1}}{\kappa' h'}}\right)\right) \tag{7}$$

On the basis of the reversible actuation in multiple dehydration and hydration cycles, we postulate that plastic deformation remains unchanged during the whole transformation process. This leads to a simple relationship between κ' and κ, such that

$$\kappa' h' = \kappa h \tag{8}$$

Combining equations (7) and (8), we can have

$$\frac{\kappa_d}{\kappa_w} = \frac{h}{h'} \tag{9}$$

Regarding the bending curvature in the case with stiffening, defined in equation (3), it contains not only κh but also two more dimensionless variables, $\frac{y_4}{h}$ and $\frac{y_2}{h}$, making the analysis more complicated than the ideal plastic case in our simple model. As y'_2 and y'_4 will change proportionally to h (Supplementary Fig. 17), this leads to $\frac{y_4}{h} = \frac{y'_4}{h'}$ and $\frac{y_2}{h} = \frac{y'_2}{h'}$. Therefore, the same relationship in equation (9) also holds for the cases with stiffening.

Equation (9) can account for around a 25% increase in the curvature from the wet to the dry state; as the thickness decreases it is about 20%. This is still lower than the experimental observation of the curvature ratio (about 2.0 in Fig. 2h). We next examined the gradient length change during drying, which can be attributed to a strain-dependent shrinkage during dehydration and has been reported in previous studies[53,54]. To simplify our analysis, we first decoupled this effect with the thickness change and assumed that the thickness keeps a constant value. Here we assumed that the non-uniform shrinkage is proportional to the mechanical strain in the wet state

$$\epsilon_w = \epsilon_w^0 - \beta \kappa_w y \tag{10}$$

in which ϵ_w^0 denotes a constant shrinkage, β is an empirical parameter that describes the coupling between the mechanical strain and shrinkage, y is the coordinate along the thickness direction and $\kappa_w y$ characterizes the mechanical strain distribution. Note that we compared the curvatures at the two end states and neglected the kinetic effects. In principle, β will also depend on the strain values. Here, as our focus was to identify the key actuation mechanism, a constant value of β is preferred for deriving a closed-form solution. A numerical solution to address the dynamic process will be investigated in the future[54]. After taking the shrinkage strain, the stress in the dry state σ_d should be modified as

$$\sigma_d = \sigma_w - \epsilon_w E \tag{11}$$

in which σ_w is the stress in the wet state and described in equations (8) and (15) in Supplementary Note 9. The corresponding equilibrium equations are

$$\int_{-\frac{h}{2}}^{\frac{h}{2}} \sigma_d \mathrm{d}y = \int_{-\frac{h}{2}}^{\frac{h}{2}} \sigma_w \mathrm{d}y - (E\epsilon_w^0 h) = 0 \tag{12}$$

and

$$\int_{-\frac{h}{2}}^{\frac{h}{2}} \sigma_d y \mathrm{d}y = \int_{-\frac{h}{2}}^{\frac{h}{2}} \sigma_w y \mathrm{d}y + \frac{1}{12}\beta \kappa_w E h^3 \tag{13}$$

It is interesting to note that the non-uniform shrinkage strain only adds one constant term to the existing equations. The dry curvature can be solved from equation (13) as

$$\frac{\kappa_d}{\kappa} = \frac{\kappa_w}{\kappa}(1+\beta) \tag{14}$$

Now we can directly express the curvature ratio between the dry and the wet state as

$$\frac{\kappa_d}{\kappa_w} = 1 + \beta \tag{15}$$

The same argument relating to the thickness shrinkage effect can be applied to the dry sample. Therefore, we can further superimpose the thickness shrinkage to the curvature to give a final curvature ratio of

$$\frac{\kappa_d}{\kappa_w} = (1+\beta)\frac{h}{h'} \tag{16}$$

Modelling and simulations of the coiling and drilling of the engineering seed carrier

The fabrication and actuation of coiling actuators are more complicated to model than the bending actuators, although they share the same fundamental mechanism. The difficulties stem from the nonlinear and coupled plastic behaviours and strain-dependent shrinkage induced by moisture change in three-dimensional coils. On the other hand, the mechanical behaviours of coiling actuators are generally determined by coiling stiffness and coiling configuration change, including the coiling elongation and rotation (equation (1)). This motivates us to choose a phenomenological model capable of capturing the configuration change and the associated extension forces of wood coils during hydration and dehydration cycles. A simpler model is also preferred to achieve our goal of simulating the drilling performance of the seed carriers, which requires modelling of the complex structural design and highly nonlinear interactions between the seed carriers and soils.

The phenomenological model for the formation and actuation of the wood coils is inspired by the manufacturing and deployment of the wood-based seed carriers (Supplementary Note 10). The coiling and uncoiling processes of wood veneers are modelled as shape morphing of a mechanically anisotropic strip, driven by anisotropic contraction and expansion, which mimic the effect of moisture change (Supplementary Note 10). The model is implemented in ABAQUS/Implicit with spatially non-uniform hydration or dehydration strain, defined as an anisotropic thermal expansion or contraction. The wood strip starts from an initially flat state with its thickness, width and length matching the experimental sample. The water transport is not directly modelled. Instead, we assigned an exponential time variation of the hydration strain with a characteristic timescale. The hydration strain field and characteristic timescale are fitted with the coiling configuration (for example, coil diameter and pitch) of hydrated coils in a controlled humidity chamber (Supplementary Note 11). The mechanical properties of the modelled material were obtained by fitting the measured moisture-dependent modulus and the extension forces of the coils (Supplementary Note 11).

We then developed simulation models for the drilling process of seed carriers in relation to both body and tails (Fig. 3b–e and Supplementary Note 12). The soil surface was treated as a rigid flat surface, which interacts with the seed carrier body and tails through normal contact and frictional forces (Supplementary Fig. 26). The effect of deformability and roughness of the soil surfaces will be lumped into effective coefficients of friction between the surfaces of the seed body and tip and the soil surface. Our experiments show that the tails and seed tip can penetrate the soil surfaces to form anchoring points. To mimic tail anchoring, we set a higher coefficient of friction at a small region near the tail tip. The seed tip is not included in the simulation model, as it is challenging to connect the tip with a non-stress-free coiled body. We further introduced a normalized hydration state to describe the transition of the coils from the dry to the wet state in Fig. 3b,c (equation (26) in Supplementary Note 12). We show that the effects of the tip anchoring can be partially explained by fixing the in-plane motion of one point of the coiled body, which closely reproduces the corresponding drilling processes in experiments (Fig. 3d,e) on coconut coir with a LSMV of 1.62 mm^2. We conducted further experiments and simulations of seed carrier drilling on a surface that was hard and smooth (Supplementary Note 12) and found a substantial rotation of the seed carriers, due to the low frictional force and lack of anchoring points

(Extended Data Fig. 9). The three-tailed design rotated less than the single-tailed design, as it can establish contact not only at two tails but also at the seed tip, owing to the initially inclined angle on the surface. This further validates that our simulations can capture the interaction between engineered seed carriers and different ground types, despite the simplification of the model.

The model is relatively simple and has its own limitations. Nevertheless, it is sufficient for our current analysis, as shown by the agreements between modelling prediction and experimental measurements. More theoretical studies are needed to establish the relationship between the change of pitch and curvature of the coiling actuators and the structures, and the mechanical properties of wood strips. It is also desirable to incorporate the microstructures (for example, cellular networks and MFA) and their nonlinear interactions into the numerical simulation framework of the coiling and drilling process, to enhance the predictivity of the model for a variety of material systems. Furthermore, water transport inside the wood strips has been shown to play a critical role in determining the dynamic morphing process of hygroscopically actuated structures[55,56]. This will require integration of the current pure mechanical model in a proper kinetic model for moisture permeation in the wood in the future, to better capture real seed carrier actuation driven by water transport.

Reporting summary

Further information on research design is available in the Nature Portfolio Reporting Summary linked to this article.

Data availability

Data generated and analysed during the study is available at https://doi.org/10.5281/zenodo.7057562. Digital models, processing protocols and datasets are available on request from L.Y.

Code availability

Code used for the finite-element analysis to simulate coil extension and drilling is available at https://doi.org/10.5281/zenodo.7263943. Further information on code and models used is available on request from T.Z.

49. Stamp, N. E. Seed dispersal of four sympatric grassland annual species of *Erodium*. *J. Ecol.* **77**, 1005 (1989).
50. Freckman, D. W. & Virginia, R. A. Low-diversity Antarctic soil nematode communities: distribution and response to disturbance. *Ecology* **78**, 363–369 (1997).
51. Yang, N., Li, T. & Zhang, L. A two-dimensional lattice model for simulating the failure and fracture behavior of wood. *Wood Sci. Technol.* **54**, 63–87 (2020).
52. Reiterer, A. & Stanzl-Tschegg, S. E. Compressive behaviour of softwood under uniaxial loading at different orientations to the grain. *Mech. Mater.* **33**, 705–715 (2001).
53. Hanhijärvi, A. Advances in the knowledge of the influence of moisture changes on the long-term mechanical performance of timber structures. *Mater. Struct.* **33**, 43 (2000).
54. Fortino, S., Mirianon, F. & Toratti, T. A 3D moisture-stress FEM analysis for time dependent problems in timber structures. *Mech. Time Depend. Mater.* **13**, 333 (2009).
55. Lunni, D., Cianchetti, M., Filippeschi, C., Sinibaldi, E. & Mazzolai, B. Plant-inspired soft bistable structures based on hygroscopic electrospun nanofibers. *Adv. Mater. Interfaces* **7**, 1901310 (2020).
56. Krüger, F. et al. Development of a material design space for 4D-printed bio-inspired hygroscopically actuated bilayer structures with unequal effective layer widths. *Biomimetics* **6**, 58 (2021).

Acknowledgements We thank C. Y. Wei for processing suggestions, E. Sharon for mechanism discussions, and L. B. Hu, J. Z. Gu and J. Forman for helpful insights. We also thank J. Y. Zhu and N. Z. Plaza from the US Department of Agriculture Forest Products Laboratory for discussions and characterization through X-ray diffraction. We acknowledge funding support from the US National Science Foundation, including IIS-CAREER-1847149 (L.Y.), CMMI-2020476 (T.Z.) and the Future Eco Manufacturing Research Grant, no. CMMI 2037097 (S.Y.). Simulations were carried out at the Triton Shared Computing Cluster at the San Diego Supercomputer Center and the Expanse cluster (TG-MSS170004, T.Z.) in the Extreme Science and Engineering Discovery Environment. We also acknowledge the use of the Materials Characterization Facility at Carnegie Mellon University (MCF-677785, L.Y.), the National Natural Science Foundation of China (62002321, G.W.) and a gift to Carnegie Mellon University (L.Y.) from Accenture Labs.

Author contributions L.Y. and D.L. conceived the initial concept. A.M. and A.D. conceived two application contexts. L.Y., T.Z., S.Y. and G.W. supervised the project. L.Y., D.L., T.Z. and S.Y. wrote the manuscript. D.L., L.Y. and G.W. carried out fabrication and peak force measurements. D.L., L.Y., G.W., J.L., Y.Y., Y.T. and L.S. carried out drilling and germination tests. D.L., L.Y. and Y.Y. carried out bending angle and coil pitch measurements. D.L., L.Y. and D.K.P. carried out scanning electron microscopy and micrograph analysis. D.K.P. and L.Y. conducted tensile tests. T.Z. and L.Y. carried out curvature analysis. T.Z. carried out mechanical modelling and simulation. S.Y., T.Z. and L.Y. provided scientific and experimental advice. L.Y. and D.L. created the videos.

Competing interests A US patent application (application no. 17/718,232) on the methods and devices for the biomimetic composite has been filed by Carnegie Mellon University (assignors: L.Y., G.W., J. Gu, D.L. and F. Qin.). The other authors declare no competing interests.

Additional information
Supplementary information The online version contains supplementary material available at https://doi.org/10.1038/s41586-022-05656-3.

Correspondence and requests for materials should be addressed to Guanyun Wang, Shu Yang, Teng Zhang or Lining Yao.

Peer review information *Nature* thanks Barbara Mazzolai, Naomi Nakayama and the other, anonymous, reviewer(s) for their contribution to the peer review of this work. Peer reviewer reports are available.

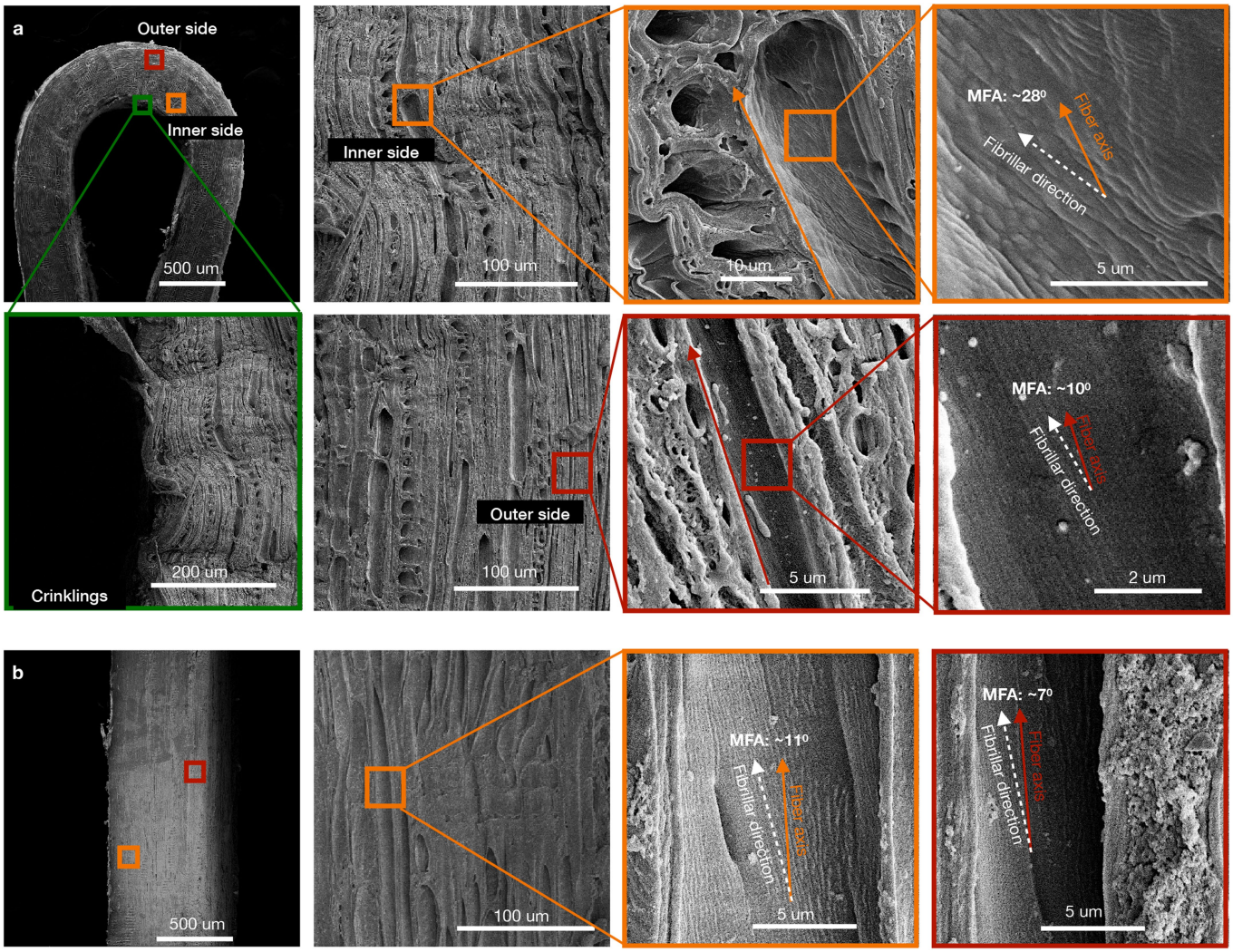

Extended Data Fig. 1 | SEM images of partially delignified wood veneer. **a**, Chemically washed and moulded wood veneer (0.5 mm thick, 0.8 mm mandrel diameter). Wrinkled cell walls are caused by mechanical moulding on the longitudinal cells on the inner side. The outer side cells show no obvious signs of deformation. **b**, The chemically washed but not moulded wood veneer, showing uniform cell structure throughout the sample.

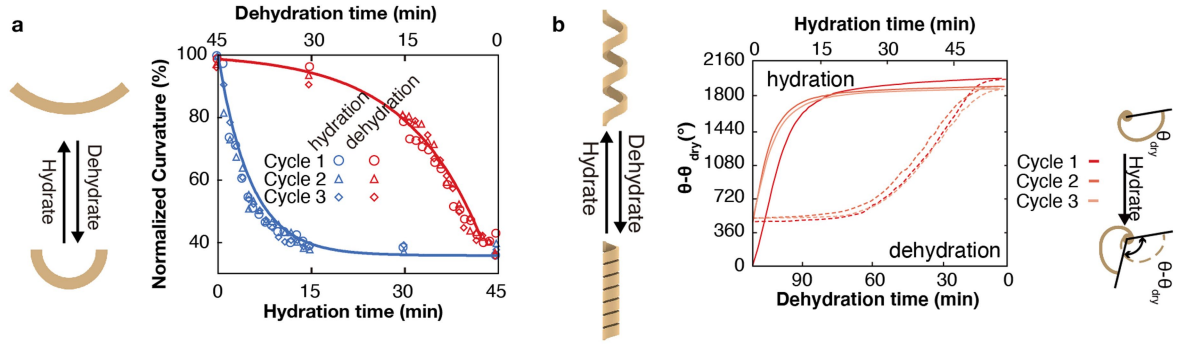

Extended Data Fig. 2 | Performance of the engineered moisture-driven actuators. a, Reversible curvature changes of a bending actuator during three actuation cycles. **b**, Reversible actuation of a moulded coiling actuator with seven coils in three consecutive hydration-dehydration cycles, showing the angular changes relative to the initial position of the top end of the helix (θ-θ_{dry}). Both actuators are 3 mm in width and 0.5 mm in thickness, moulded with a mandrel, with a 0.8 mm diameter. The length is 3 mm in (a) and 40 mm in (b).

Extended Data Fig. 3 | Design of a remote-controlled device that can be attached to a drone to carry and deploy seeds. a, Photograph of the customized seed deployment mechanism attached to a drone. **b**–**d**, Top view of the device with a sliding cover to prevent turbulence caused by the wings of the drone from affecting the deployment. **e**–**f**, Bottom view of the device, with a magnetic double-side door that can be opened with a remote-controlled pulling mechanism, shown in (**g**). **h**–**j**, A field test of the aerial delivery with examination of the landing pose of the seed carriers. **k**–**l**, a portion of the seed carriers for the aerial delivery test. The tails are dyed with bright colors for easy identification. Scale bar: 10 mm.

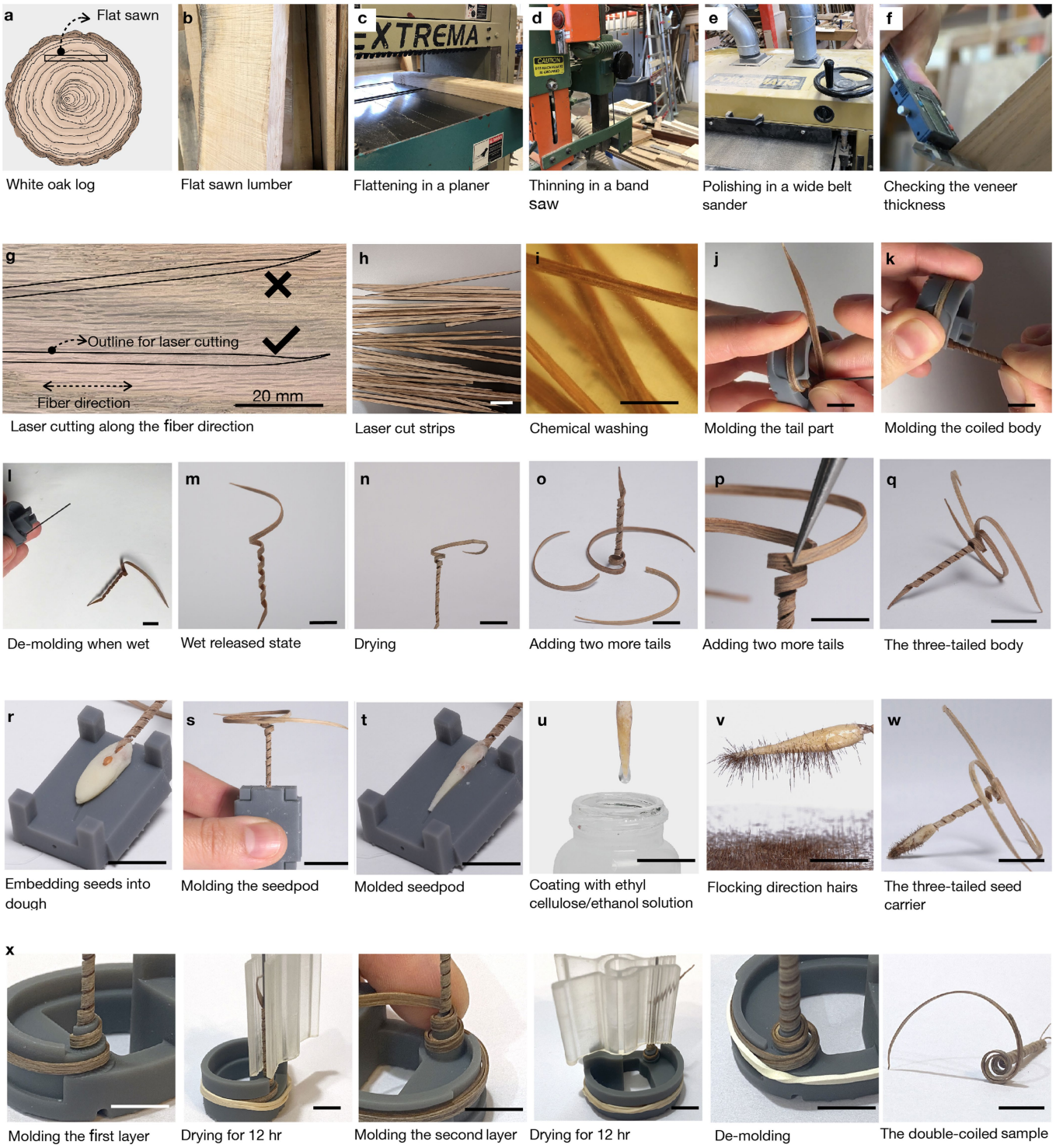

Extended Data Fig. 4 | Photos of the fabrication and assembly of the seed carrier prototypes. a–**f**, The process of turning a white oak log into a wood veneer with a specified thickness and fiber orientation. **g**–**h**, The process of laser cutting, chemical washing and manual moulding of the wood strips. **i**, The chemical washing process. **j**–**n**, The mechanical moulding process. **o**-**q**, Adding two additional tails for three-tailed seed carriers. **r**–**w**, The tip manufacturing process adapted from the literature[24] with additional seeds embedding. **x**, The process of moulding a double-coiled body. Scale bar is 10 mm unless otherwise specified.

Extended Data Fig. 5 | Comparison of the self-drilling depth between a double-coiled and a single-coiled seed carrier. a–**b**, Photographs of four cycles of a double-coiled seed carrier (**a**) and a single-coiled seed carrier (**b**) at each hydration and dehydration state.

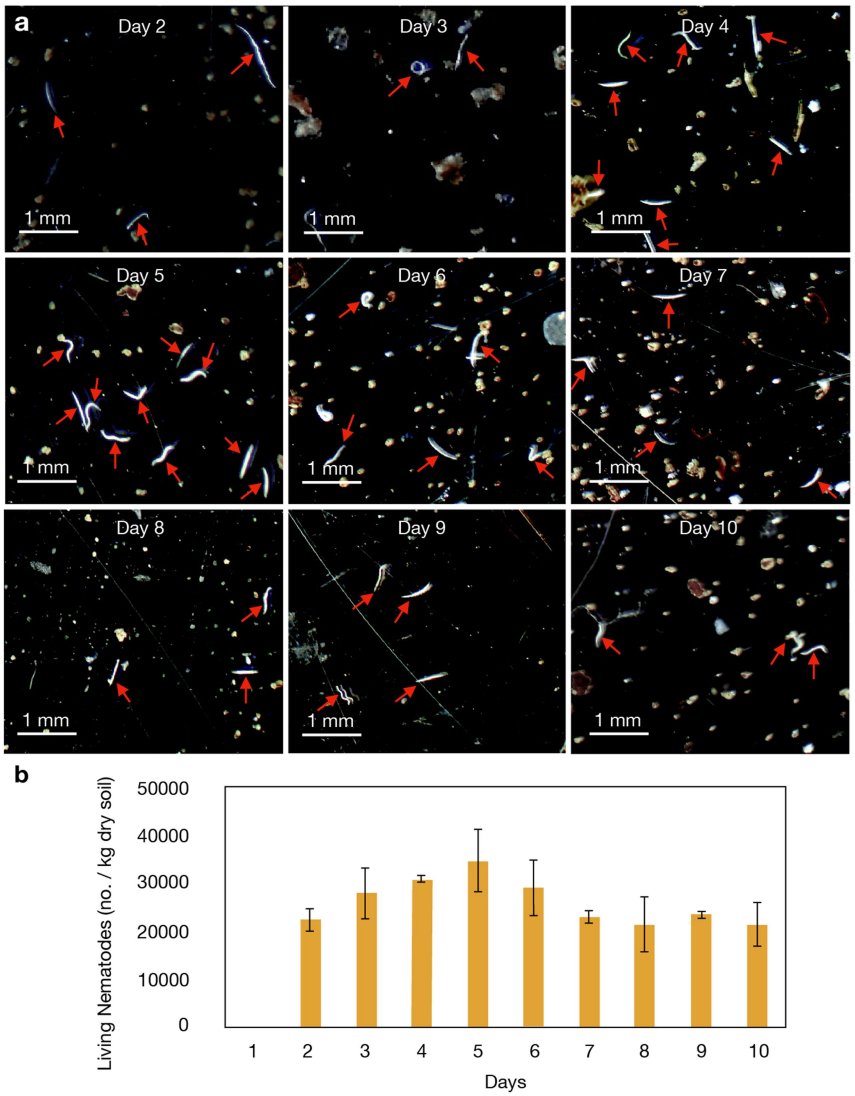

Extended Data Fig. 6 | Tracking of the living nematodes extracted from the soil. a, Representative images of nematodes extracted from the soil (Methods). **b**, The total number of living nematodes identified in the soil samples. Data are means ± s.d. $n = 3$ soil samples each day.

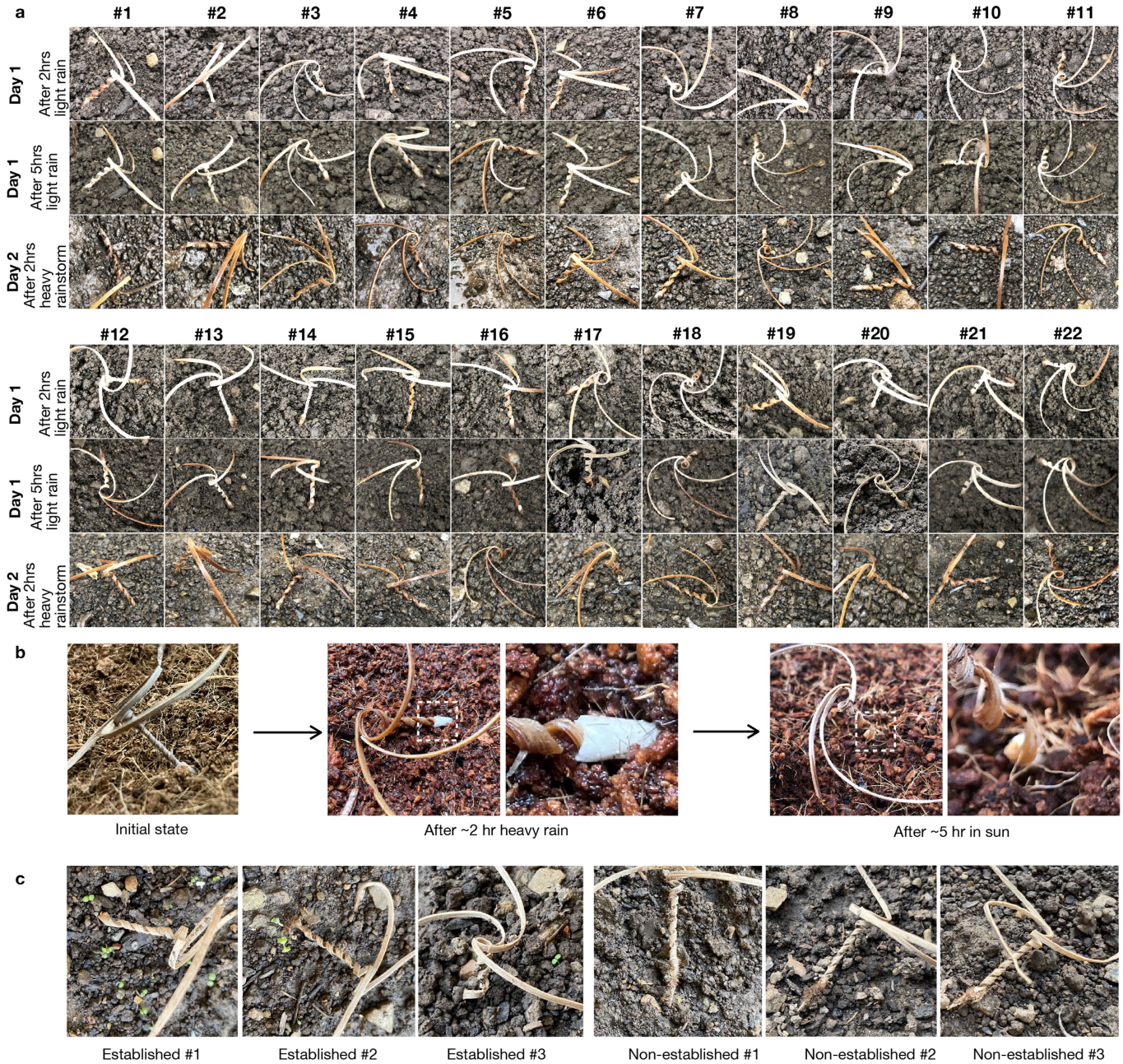

Extended Data Fig. 7 | Selective field drilling and germination test results (more details in Supplementary Table 5). a, Drilling test 1 from Table S5, with 22 three-tailed seed carriers under natural conditions for two consecutive days. **b**, A rain-anchored seed continues to drill after the sun emerges, as shown in drilling test 3 of Table S5. **c**, Established seed carriers tend to germinate more easily than non-established seed carriers after five days with four periods of rain. The established and exposed seeds had a 100% and 19% germination rate, respectively, in drilling test 1 of Supplementary Table 5.

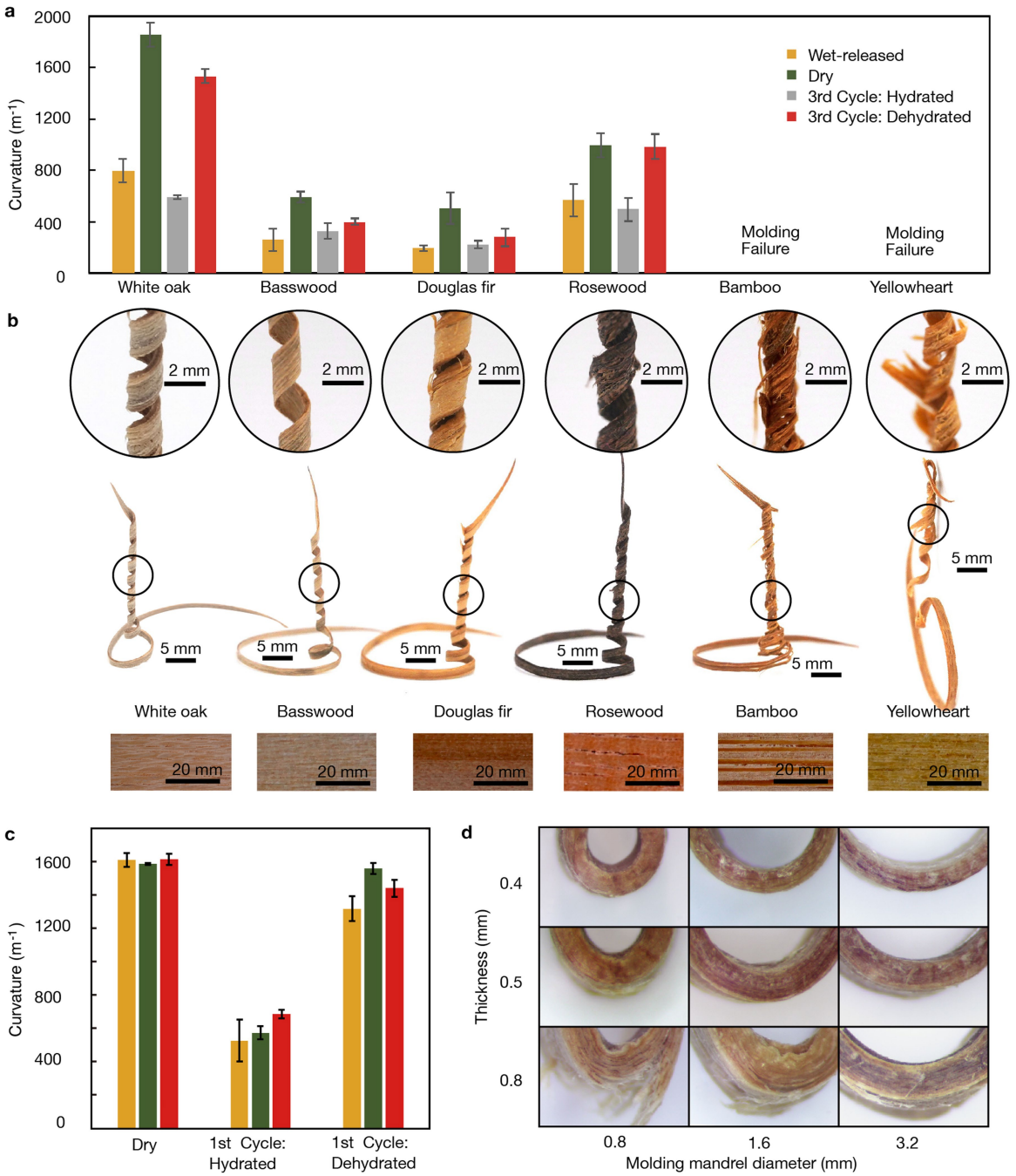

Extended Data Fig. 8 | Optimizing the material choice and processing method. a, Comparison of the mouldability and actuation range of bending actuators made of different types of wood. The wood strip is ~0.5 mm thick and the moulding diameter is 0.8 mm. Data are means ± s.d. $n = 3$ samples for each type of wood. **b**, Comparison of the mouldability of the seed body made of various types of wood. The wood strip is ~0.5 mm thick. **c**, Effect of the chemical washing durations on the curvature changes. For both (**a**) and (**c**), data are means ± s.d. $n = 3$ with a thickness of ~0.5 mm, length of ~3 mm and width of ~3 mm, moulded with a mandrel with a 0.8 mm diameter. **d**, Moulding quality comparison on wood veneer of different thickness, moulded on mandrels of different diameters, with a washing duration of 10 min.

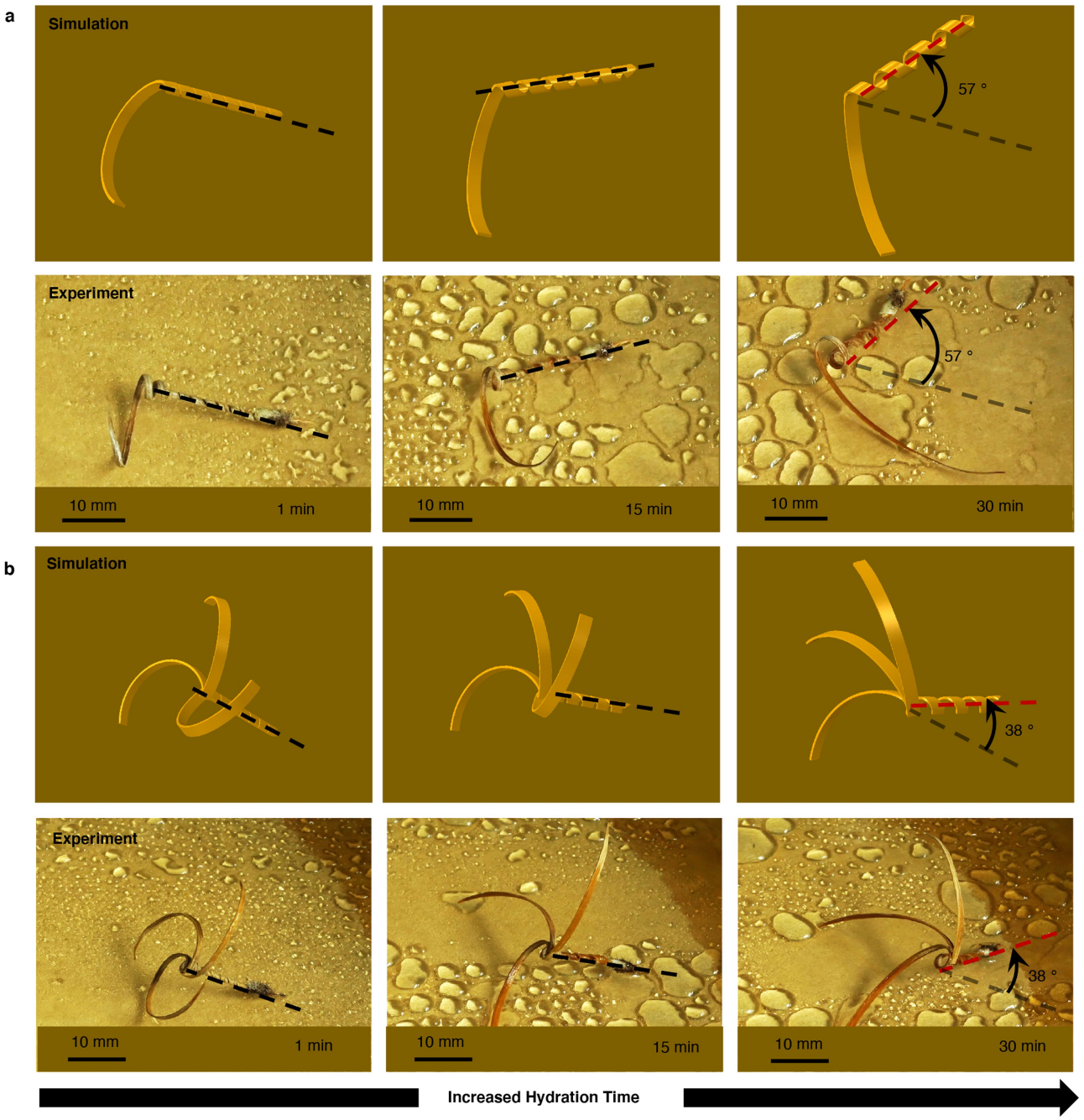

Extended Data Fig. 9 | Experiments and simulations for seed carrier drilling on a surface that is hard and smooth. a, Simulation (top) and experimental (bottom) snapshots of the drilling process of the single-tailed design seed carrier. **b**, Simulation (top) and experimental (bottom) snapshots of the drilling process of the three-tailed design seed carrier.

nature portfolio

Corresponding author(s): Guanyun Wang, Shu Yang, Teng Zhang, Lining Yao

Last updated by author(s): Sep 15, 2022

Reporting Summary

Nature Portfolio wishes to improve the reproducibility of the work that we publish. This form provides structure for consistency and transparency in reporting. For further information on Nature Portfolio policies, see our Editorial Policies and the Editorial Policy Checklist.

Statistics

For all statistical analyses, confirm that the following items are present in the figure legend, table legend, main text, or Methods section.

n/a	Confirmed	
☐	☒	The exact sample size (*n*) for each experimental group/condition, given as a discrete number and unit of measurement
☐	☒	A statement on whether measurements were taken from distinct samples or whether the same sample was measured repeatedly
☐	☒	The statistical test(s) used AND whether they are one- or two-sided *Only common tests should be described solely by name; describe more complex techniques in the Methods section.*
☐	☒	A description of all covariates tested
☐	☒	A description of any assumptions or corrections, such as tests of normality and adjustment for multiple comparisons
☐	☒	A full description of the statistical parameters including central tendency (e.g. means) or other basic estimates (e.g. regression coefficient) AND variation (e.g. standard deviation) or associated estimates of uncertainty (e.g. confidence intervals)
☒	☐	For null hypothesis testing, the test statistic (e.g. *F*, *t*, *r*) with confidence intervals, effect sizes, degrees of freedom and *P* value noted *Give P values as exact values whenever suitable.*
☒	☐	For Bayesian analysis, information on the choice of priors and Markov chain Monte Carlo settings
☐	☒	For hierarchical and complex designs, identification of the appropriate level for tests and full reporting of outcomes
☒	☐	Estimates of effect sizes (e.g. Cohen's *d*, Pearson's *r*), indicating how they were calculated

Our web collection on statistics for biologists contains articles on many of the points above.

Software and code

Policy information about availability of computer code

Data collection	Commercial software including Microsoft Excel, Keynote and ABAQUS are used for data collection.
Data analysis	Commercial software including Microsoft Excel, Matlab, ImageJ and Kappa Curvature Analysis plugin are used for data analysis.

For manuscripts utilizing custom algorithms or software that are central to the research but not yet described in published literature, software must be made available to editors and reviewers. We strongly encourage code deposition in a community repository (e.g. GitHub). See the Nature Portfolio guidelines for submitting code & software for further information.

Data

Policy information about availability of data

All manuscripts must include a data availability statement. This statement should provide the following information, where applicable:

- Accession codes, unique identifiers, or web links for publicly available datasets
- A description of any restrictions on data availability
- For clinical datasets or third party data, please ensure that the statement adheres to our policy

Data generated and analyzed during the study is available at doi.org/10.5281/zenodo.7057562, and the code for generating the coiled body and simulating the drilling process are available upon request. Correspondence and requests for materials, digital models, processing protocols and dataset should be addressed to guanyun@zju.edu.cn, shuyang@seas.upenn.edu, tzhang48@syr.edu, liningy@andrew.cmu.edu.

Field-specific reporting

Please select the one below that is the best fit for your research. If you are not sure, read the appropriate sections before making your selection.

☒ Life sciences ☐ Behavioural & social sciences ☐ Ecological, evolutionary & environmental sciences

For a reference copy of the document with all sections, see nature.com/documents/nr-reporting-summary-flat.pdf

Life sciences study design

All studies must disclose on these points even when the disclosure is negative.

Sample size	For the Erodium drilling test, the sample size is 15. For the drilling test of other natural grass seeds, the sample size is 5. For the dimensional measurements of all natural seeds, the sample size is 3. No sample-size calculation was performed.
Data exclusions	No data were excluded from the analysis.
Replication	The drilling tests in controlled conditions were reliably reproduced. In the dimensional measurements, the average and standard deviation were reported for each species.
Randomization	The seeds used in each test were randomly chosen among each species.
Blinding	The investigator were blinded to the biological sample group allocations. For the grass seeds, all drilling assessment were conducted by the blinded investigator without informing type, hygromorphic behavior or suitable habitat where the species grow.

Reporting for specific materials, systems and methods

We require information from authors about some types of materials, experimental systems and methods used in many studies. Here, indicate whether each material, system or method listed is relevant to your study. If you are not sure if a list item applies to your research, read the appropriate section before selecting a response.

Materials & experimental systems

n/a	Involved in the study
☒	☐ Antibodies
☒	☐ Eukaryotic cell lines
☒	☐ Palaeontology and archaeology
☐	☒ Animals and other organisms
☒	☐ Human research participants
☒	☐ Clinical data
☒	☐ Dual use research of concern

Methods

n/a	Involved in the study
☒	☐ ChIP-seq
☒	☐ Flow cytometry
☒	☐ MRI-based neuroimaging

Animals and other organisms

Policy information about studies involving animals; ARRIVE guidelines recommended for reporting animal research

Laboratory animals	The study did not involve laboratory animals.
Wild animals	The study did not involve wild animals.
Field-collected samples	The study did not involve samples collected from the field.
Ethics oversight	No ethical approval or guidance was required. For the organisms used in the study (i.e., various grass seeds), we purchased them directly from commercial seed suppliers.

Note that full information on the approval of the study protocol must also be provided in the manuscript.